



Cite this: *Lab Chip*, 2016, **16**, 10

## Fundamentals and applications of inertial microfluidics: a review†

Jun Zhang,<sup>a</sup> Sheng Yan,<sup>a</sup> Dan Yuan,<sup>a</sup> Gursel Alici,<sup>a</sup> Nam-Trung Nguyen,<sup>\*b</sup> Majid Ebrahimi Warkiani<sup>c</sup> and Weihua Li<sup>\*a</sup>

In the last decade, inertial microfluidics has attracted significant attention and a wide variety of channel designs that focus, concentrate and separate particles and fluids have been demonstrated. In contrast to conventional microfluidic technologies, where fluid inertia is negligible and flow remains almost within the Stokes flow region with very low Reynolds number ( $Re \ll 1$ ), inertial microfluidics works in the intermediate Reynolds number range ( $\sim 1 < Re < \sim 100$ ) between Stokes and turbulent regimes. In this intermediate range, both inertia and fluid viscosity are finite and bring about several intriguing effects that form the basis of inertial microfluidics including (i) inertial migration and (ii) secondary flow. Due to the superior features of high-throughput, simplicity, precise manipulation and low cost, inertial microfluidics is a very promising candidate for cellular sample processing, especially for samples with low abundant targets. In this review, we first discuss the fundamental kinematics of particles in microchannels to familiarise readers with the mechanisms and underlying physics in inertial microfluidic systems. We then present a comprehensive review of recent developments and key applications of inertial microfluidic systems according to their microchannel structures. Finally, we discuss the perspective of employing fluid inertia in microfluidics for particle manipulation. Due to the superior benefits of inertial microfluidics, this promising technology will still be an attractive topic in the near future, with more novel designs and further applications in biology, medicine and industry on the horizon.

Received 25th September 2015,  
Accepted 3rd November 2015

DOI: 10.1039/c5lc01159k

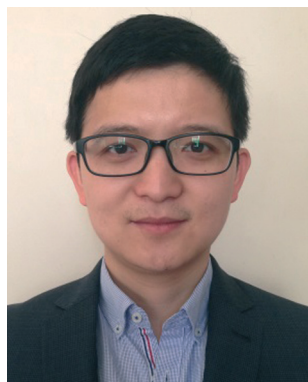
[www.rsc.org/loc](http://www.rsc.org/loc)

<sup>a</sup> School of Mechanical, Materials and Mechatronic Engineering, University of Wollongong, Wollongong, NSW 2522, Australia

<sup>b</sup> Queensland Micro- and Nanotechnology Centre, Griffith University, Brisbane QLD 4111, Australia

<sup>c</sup> School of Mechanical and Manufacturing Engineering, Australian Centre for NanoMedicine, University of New South Wales, Sydney, NSW 2052, Australia

† Electronic supplementary information (ESI) available. See DOI: 10.1039/c5lc01159k



**Jun Zhang**

*Jun Zhang received his bachelor's degree in engineering from the Nanjing University of Science and Technology (NJUST), Nanjing, China, in 2009 with an Outstanding Graduate award and received a PhD degree in mechanical engineering from University of Wollongong, Australia, in 2015. His research interests include but are not limited to 1) exploring novel techniques for micro/nano-fluidic fabrication; 2) investigating the fundamental mechanism of inertial focusing and expanding its application on bio-particle filtration, separation/sorting and ordering for bio-sample preparation and disease diagnosis; 3) developing hybrid real-time controllable inertial microfluidic systems for flexible bio-particle manipulation.*

*Published on 03 November 2015. Downloaded on 5/8/2023 7:29:27 PM.*

## 1 Introduction

Microfluidics is referred to as the science that deals with the behaviour, precise control and manipulation of fluids and particles in the scale of tens to hundreds of micrometres.<sup>1</sup>



**Sheng Yan**

*Sheng Yan received his bachelor's degree in engineering with an Outstanding Graduate award from China University of Mining and Technology in 2012. He currently holds a position as a PhD candidate in the School of Mechanical, Materials and Mechatronic Engineering at University of Wollongong. His main research focus is to develop hybrid techniques to tune hydrophoresis for cell focusing and separation. His research interests include dielectrophoresis, hydrophoresis, magnetophoresis, neurosciences, and computational fluid dynamics (CFD).*

Microfluidics is also considered as a platform for biomedical and chemical applications, called lab-on-a-chip (LOC), or micro total analysis systems ( $\mu$ TAS).<sup>2</sup> Benefiting from the precise control and manipulation of biological particles and their surrounding microenvironment, this fascinating technology holds superior advantages compared to conventional macro-scale platforms (e.g. centrifuge, flow cytometry, etc.). Microfluidics benefits include but are not limited to (i) reduced sample and reagent volumes, (ii) fast sample processing, (iii) high sensitivity, (iv) low cost, (v) improved portability, and (vi) the potential to be highly integrated and automated to reduce human intervention and error.<sup>3</sup>

Precise manipulation such as focusing, separation and fractionation of bio-particles is an indispensable capability of microfluidics. For instance, three-dimensional focusing and ordering of micro-particles along a single line allow for

single-cell level detection and analysis, which is an important component of on-chip flow cytometry. Furthermore, separation of micro-particles or cells according to their unique biophysical signatures such as size, density, shape, deformability, and surface proteins allows for a wide range of applications such as preparation of biological sample (e.g., blood, lymphatic tissue, tissue digestates, etc.) and isolation and enrichment of target cells as well as water purification.<sup>4,5</sup>

A number of technologies have already been proposed and developed to manipulate particles in microfluidic systems. According to the source of the manipulating forces, these technologies can be categorised as active and passive types. Active technologies such as dielectrophoresis (DEP),<sup>6</sup> magnetophoresis (MP),<sup>7</sup> acoustophoresis (AP)<sup>8</sup> and optical tweezer<sup>9</sup> rely on external force fields, whereas passive technologies depend entirely on the channel geometry or intrinsic



Dan Yuan

*Dan Yuan received her bachelor's degree in engineering and master's degree in engineering from Hefei University of Technology in 2011 and 2014, respectively, and majored in Precision Measurement Technology and Instruments. She currently holds a position as a PhD candidate in the School of Mechanical, Materials and Mechatronic Engineering at University of Wollongong. Her main research focus is to manipulate particles/cells in viscoelastic fluids to do focusing and separation.*



Majid Ebrahimi Warkiani

*design and development of new platforms for rare cells sorting and the development of novel 3D devices for investigation of angiogenesis and tumour formation, and (ii) bio-MEMS involving the fabrication and characterisation of novel isopore membranes as well as PCR biochips.*



Nam-Trung Nguyen

*Nam-Trung Nguyen is a professor and the director of Queensland Micro- and Nanotechnology Centre, Griffith University, Australia. He received his Dipl.-Ing., Dr.-Ing. and Dr.-Ing. Habil. degrees from the Chemnitz University of Technology, Germany, in 1993, 1997 and 2004, respectively. He was a postdoctoral research engineer at the Berkeley Sensor and Actuator Center, University of California, Berkeley, USA. From 1999 to 2013 he was*

*a research fellow, assistant professor and associate professor at Nanyang Technological University, Singapore. Dr. Nguyen has published over 240 journal papers and several books on microfluidics and nanofluidics.*



Weihua Li

*Weihua Li is a Professor with the School of Mechanical, Materials and Mechatronic Engineering of University of Wollongong, Australia. He received his B. E. and M. E. degrees from University of Science and Technology of China in 1992 and 1995, respectively, and Ph.D. degree from Nanyang Technological University (NTU) in 2001. He was a research fellow with NTU from 2001 to 2003. He has been with the University of Wollongong as a Lecturer (2003–2005), Senior Lecturer (2006–2009), Associate Professor (2010–2012), and Professor (2012–). Dr Li's research interests include but are not limited to magnetorheological materials and their applications, microfluidics and nanofluidics.*

hydrodynamic forces, such as pinched flow fractionation (PFF),<sup>10</sup> deterministic lateral displacement (DLD)<sup>11</sup> and inertial microfluidics.<sup>4</sup> An active technology generally allows for a more precise control of target particles as well as being tuneable in real time. However, the flow speed is always limited because the external force field should overcome the hydrodynamic drag to achieve effective functionality. In contrast, a passive microfluidic technology is always very simple and robust and works with a relatively higher flow rate.

Among passive microfluidic technologies, inertial microfluidics has recently attracted great attention due to its precise manipulation, simple structure and high throughput. In contrast to the common sense that, in microfluidics, fluid inertia is negligible (Stokes flow regime,  $\text{Re} \rightarrow 0$ ,  $\text{Re} = \rho_f U H / \mu$ , where  $\rho_f$ ,  $U$  and  $\mu$  are the fluid density, average velocity and dynamic viscosity, respectively, and  $H$  is the characteristic channel dimension), inertial microfluidics works in an intermediate range ( $\sim 1 < \text{Re} < \sim 100$ ) between Stokes regime and turbulent regime ( $\text{Re} \sim 2000$ ), where both inertia and viscosity of the fluid are finite. The finite inertia of the fluid brings about several intriguing inertial effects that form the basis of inertial microfluidics including (i) inertial migration and (ii) secondary flow.

Inertial migration is a phenomenon where randomly dispersed particles in the entrance of a straight channel migrate laterally to several equilibrium positions after a long enough distance, which was first observed more than 50 years ago.<sup>12,13</sup> After the first observation of inertial migration, a number of experimental studies and theoretical analyses were conducted to explore the underlying mechanism of this phenomenon.<sup>14–21</sup> This phenomenon had not found its practical application until the emergence of microfluidic technology, where particle size is comparable with the characteristic dimension of a microchannel. The inertial migration phenomenon has been widely recognised by the counteraction of two inertial effects: 1) the shear gradient lift force  $F_{LS}$ , due to the curvature of the fluid velocity profile and its interaction with a particle, which directs particles away from the channel centre, and 2) the wall lift force  $F_{LW}$ , a result of the flow field interaction between the suspending particle and the adjacent walls, which repels the particle away from the wall. The inertial equilibrium positions of particles result from the balance between these two inertial lift forces, and they are normally around 0.6 times of the channel radius to the channel centreline in a circular channel.<sup>13,22</sup>

The secondary flow usually appears in a curved channel<sup>23</sup> or a straight channel with disturbance obstacles.<sup>24–26</sup> In a curved channel, the secondary flow is induced by a pressure gradient in the radial direction because of fluid momentum mismatch in the centre and near-wall region within the curvature.<sup>4</sup> The fluid elements near the channel centreline have a higher momentum than those near the wall, and therefore flow outwards and drive relative stagnant fluid elements near the channel wall inwards along the circumference, forming two counter-rotating streams, called Dean vortex. Introducing this secondary flow in inertial focusing brings several

benefits. For example, the Dean vortex can modify the inertial equilibrium positions by imposing an additional viscous drag force on particles perpendicular to the main stream. Size-dependent differential focusing of particles according to the ratio of inertial lift force and secondary flow drag ( $F_L/F_D$ ) promises complete particle separation. In addition, the Dean vortex could reduce the channel length/footprint due to the mixing effects of secondary flow, assisting particles to reach equilibrium position more quickly.<sup>4</sup>

In this review, we will first discuss the fundamental kinematics of micro-particles inside microchannels. We then present a comprehensive review of the recent progress of inertial microfluidics according to the structure of functional microchannels because the structure of the microchannel is the most crucial parameter that determines the functionality and performance of inertial microfluidic devices. Finally, the limitation of current investigations will be discussed. We then propose several future directions of inertial microfluidics. We hope that this review could serve as a comprehensive guide for readers who are new to the area of inertial microfluidics. For readers with a decent background, we hope that the review can provide an extended understanding of the fundamental mechanism, inspire novel device design or initiate an expanded application of inertial microfluidics.

## 2 Fundamental dynamics of particle movement in a microfluidic channel

### 2.1 Viscous drag force

Drag force arises when an object moves through a fluid or, relatively, when the fluid flows past an object. The origin of the drag force lies in the need to displace the elements of the fluid out of the way of the moving object. The drag force on a moving spherical particle can be expressed as:

$$F_{\text{drag}} = S \times f_{\text{drag}} = \pi a^2 f_{\text{drag}} / 4 \quad (1)$$

where  $S$  is the cross-sectional area of moving particles, and  $a$  is the diameter of the particle.  $f_{\text{drag}}$  is the viscous drag coefficient which is always determined by the particle Reynolds number  $\text{Re}' = v_t \rho_f a / \mu$ ; here  $v_t$  is the relative velocity of fluid to particle.<sup>27</sup>

The viscous drag coefficient  $f_{\text{drag}}$  can be divided into four sections according to the range of the particle Reynolds number  $\text{Re}'$ :<sup>27</sup>

(a) When  $10^{-4} < \text{Re}' < 0.2$

$$f_{\text{drag}} = 12 \frac{\mu v_t}{a} \quad (2a)$$

then

$$F_{\text{drag}} = 3\pi\mu a v_t \quad (2b)$$

This is actually the well-known formula of the Stokes drag, which has been widely used for analytical analysis because of

its simplicity, especially when the relative velocity of fluid to particle  $v_t$  is very small.

(b) If  $0.2 < \text{Re}' < 500 \sim 1000$

$$f_{\text{drag}} = 12 \frac{\mu v_t}{a} (1 + 0.15 \text{Re}'^{0.687}) \quad (3a)$$

then

$$F_{\text{drag}} = 3\pi\mu a v_t (1 + 0.15 \text{Re}'^{0.687}) \quad (3b)$$

(c) If  $500 \sim 1000 < \text{Re}' < 2 \times 10^5$

$$f_{\text{drag}} = 0.22 \rho_f v_t^2 \quad (4a)$$

then

$$F_{\text{drag}} = 0.055\pi a^2 \rho_f v_t^2 \quad (4b)$$

Subsequently, Khan and Richardson examined the experimental data and suggested an equation that suits values of  $\text{Re}'$  up to  $10^5$ :<sup>27</sup>

$$f_{\text{drag}} = (1.84 \text{Re}'^{-0.31} + 0.293 \text{Re}'^{0.06})^{3.45} \rho_f v_t^2 \quad (5a)$$

$$F_{\text{drag}} = \frac{\pi}{4} a^2 \rho_f v_t^2 (1.84 \text{Re}'^{-0.31} + 0.293 \text{Re}'^{0.06})^{3.45} \quad (5b)$$

In inertial microfluidics, viscous drag force is composed of two components: along 1) the mainstream direction, due to the axial velocity difference between the fluid and the suspended particles, and 2) the cross section, due to the secondary flow induced by the channel curvature or disturbance structures.

## 2.2 Diffusion

Brownian motion is the random motion of suspending particles immersed in a fluid (liquid or gas), which results from their frequent collision with the quick atoms or molecules in the gas or liquid. Diffusion is ubiquitous in particle–fluid systems. According to the Einstein–Smoluchowski theory, the mean square distance that a particle diffuses in time  $t$  is expressed as:<sup>28</sup>

$$\langle r^2 \rangle = 6Dt \quad (6)$$

where  $D$  is the diffusion coefficient. According to the Stokes–Einstein relationship, the diffusion coefficient is given as:

$$D = \frac{kT}{3\pi\mu a} \quad (7)$$

where  $k$  is the Boltzmann's constant, which is about  $1.3806488 \times 10^{-23}$  J K<sup>-1</sup>.  $T$  is the absolute temperature.<sup>28</sup> From the above equation, we can see that the higher the temperature  $T$ , the larger is the diffusion coefficient  $D$ . In contrast,

the larger the particle size  $a$  or the higher the medium viscosity  $\mu$ , the smaller is the diffusion coefficient. When the particle–fluid system is not static, but moving along the micro-channel, the Pécelt number can be employed to evaluate the relative importance of convection to diffusion:<sup>29</sup>

$$\text{Pe} = \frac{LU}{D} \quad (8)$$

where  $L$  is the characteristic dimension of the channel and  $U$  is the characteristic velocity of the fluid. The large Pécelt number indicates that convection dominates the transport of particles in the flow, while a small Pécelt number means that diffusion plays a primary role in the transport. In inertial microfluidics, diffusion is normally neglected in the analysis of microscale particle movement.

## 2.3 Magnus force – rotation-induced lift force

In an in-viscous flow with uniform velocity  $U$ , a stationary cylinder is rotating with constant angular velocity  $\vec{\Omega}$ ; see Fig. 1(a). Assuming no slip velocity at the surface of the cylinder, the fluid velocity at the bottom part is lower than the velocity at the upper part. According to the Bernoulli principle, the pressure is higher at the lower part than in the upper part of the cylinder. As a result, a lift force  $F_{\text{LR}}$  is developed to lift the cylinder. The magnitude of this lift force per unit length of the cylinder is:<sup>30</sup>

$$\vec{F}_{\text{LR}} = \pi \rho_f^2 a \vec{U} \times \vec{\Omega} \quad (9)$$

Similarly for a rigid sphere rotating in a fluid, a lateral lift force appears due to the transverse pressure difference, and this force is called “Magnus lift force”:<sup>31</sup>

$$\vec{F}_{\text{LR}} = \frac{1}{8} \pi a^3 \rho_f \vec{U} \times \vec{\Omega} \quad (10)$$

If the sphere is not stationary, but simultaneously translating through the fluid with a velocity  $\vec{u}_p$ , replacing the fluid velocity vector  $\vec{u}$  by the relative velocity ( $\vec{u}_f - \vec{u}_p$ ) results in:

$$\vec{F}_{\text{LR}} = \frac{1}{8} \pi a^3 \rho_f (\vec{u}_f - \vec{u}_p) \times \vec{\Omega} \quad (11)$$

The direction of the Magnus force is perpendicular to the plane defined by the vectors of the relative velocity and the axis of rotation. In the case of a sphere rotating with an angular velocity  $\vec{\Omega}_s$  in a rotational flow field, the vector  $\vec{\Omega}$  represents the relative rotation between the fluid and the sphere:

$$\vec{\Omega} = \vec{\Omega}_s - 0.5 \nabla \times \vec{u}_f \quad (12)$$

Magnus force can be considered as a result of the pressure difference induced by the streamline asymmetry due to the rotation of the sphere. Although the above particular

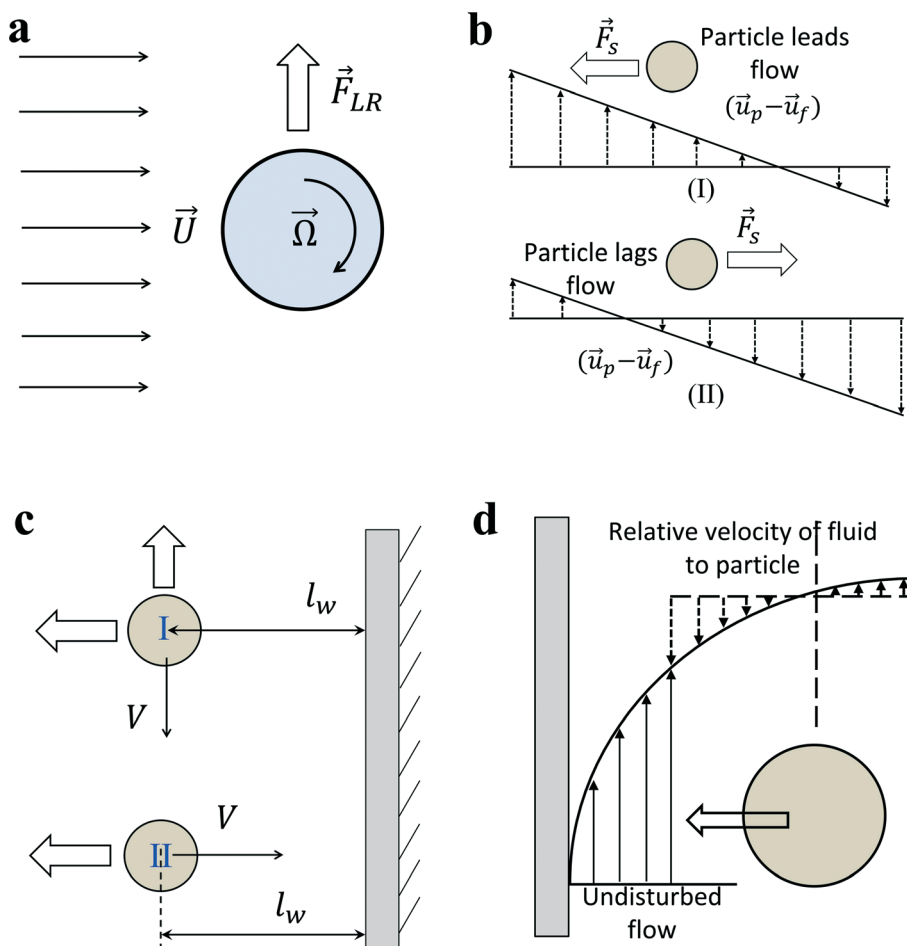


**Fig. 1** (a) Rotation induced lift force for a rigid cylinder or sphere in a uniform flow. (b) Saffman force on a sphere due to slip-shear motion in a simple shear flow. The direction of lateral lift force always directs toward the side where the magnitude of relative velocity is maximum. (c) Boundaries retard the motion of the particle no matter whether the main flow direction is parallel (I) or perpendicular (II) to the wall boundary. An additional wall lift force directs perpendicularly to the main flow direction when particles are moving parallel to the boundary. (d) Shear gradient lift force on a particle in a Poiseuille flow. In the moving frame with the particle, the relative velocity of fluid to particle is larger on the wall side due to the parabolic fluid velocity profile. Therefore, shear-gradient lift force directs toward the nearby wall.<sup>33</sup>

expressions are valid only for low Reynolds numbers, this kind of lift force due to the rotation of a body is also present in a more strongly inertial flow.<sup>32</sup> In fact, as a result of the outer velocity field disturbance by the rotation, where fluid inertia is essential, the Magnus force would not appear in the creeping flow but is present in all rotating flows with finite relative velocity no matter if it is viscous or inviscid.<sup>30</sup>

#### 2.4 Saffman force – slip-shear induced lift force

Inertial migration is an interesting phenomenon where randomly dispersed particles in the entrance of a straight micro-channel migrate laterally to a narrow annulus at about 0.6 times of the tube radii from the axis, which was first quantitatively measured by Segre and Silberberg in the 1960s.<sup>12,13</sup> After that, a series of analytical analyses and numerical simulations have been conducted to explain this counter-intuitive phenomenon.<sup>14–19</sup> However, the full problem is more complex, as not only does the effect of inertia need to be

calculated for a particle in a parabolic velocity profile but also the presence of the tube walls must be taken into account. The walls are clearly very important to the existence of the phenomenon. Without channel walls, the flow will be uniform and there is even no velocity gradient, generating no rotational motion on a force-free rigid sphere, and consequently no lateral lift force appears. The wall effects at least act in two different ways: first, the existence of walls creates a fluid velocity gradient (shear rate) and the corresponding shear-induced particle rotation. The extra drag caused by walls makes the particle lag behind the fluid. This slip-shear motion will generate a lateral force on the particles called the Saffman force. Second, the flow field around the particle is disturbed by the presence of the walls and the inertial effects will differ from those for a particle in an unbounded flow, especially when the particle is close to the walls.<sup>34</sup> Here, we focus on the first effect and only consider the force on a sphere in an unbounded simple shear flow, *i.e.* constant shear rate and zero shear gradient. The second effect of the

wall will be detailed in the section ‘‘Wall-induced lift force’’. For Poiseuille flow with non-zero shear gradient, the effects of the parabolic velocity profile on particle migration will be discussed in the section ‘‘Shear-gradient lift force’’.

Using the matched asymptotic expansion method, Saffman<sup>34</sup> calculated the lateral lift force on a sphere in a simple unbounded shear flow. The force arises from the interaction of the Stokeslet velocity field of the particle and the velocity gradient of the bulk flow. The magnitude of this force is:

$$F_S = \frac{K}{4} V a^2 (\gamma v^{-1})^{1/2} \quad (13)$$

where  $K$  is a numerical constant ( $K \sim 81.2$ ),  $\gamma$  is the velocity gradient (or shear rate),  $v$  is the kinetic viscosity and  $V$  is the relative velocity between the particle and the fluid at the streamline through the centre of the particle. It should be pointed out that this force is the only effect of shear rate, independent of the rotation of the particle. In the real situation, the spheres are free to move, and a relative rotation will be induced by the shear. Consequently, a Magnus-type force may appear on the sphere. In most practical flows, the effects of rotation and shear cannot be considered as independent, and a simple superposition of the two lift forces would inevitably bring errors.<sup>30</sup> Unless the rotation speed is much greater than the rate of shear, for a freely rotating particle

$\Omega = \frac{1}{2}\gamma$ , the Saffman force  $F_S$ , caused by the interaction of slip velocity (Stokeslet flow field) and shear, will generally be at least one order of magnitude larger than the Magnus force  $F_{LR}$  caused by the interaction of slip and particle rotation at low Reynolds numbers.<sup>32</sup>

The direction of the Saffman force is always towards the side where the magnitude of relative velocity  $V$  is maximum (Fig. 1(b)). If the particles are leading the flow, the Saffman force directs to the stagnant wall in a simple shear flow; if the particles are lagging the flow, the Saffman force points to the moving wall. In the case of a neutrally buoyant particle in a Poiseuille flow, the particle is force-free and the Stokeslet generated by the lag of the particle relative to the shear flow (slip-shear) is balanced by an opposite Stokeslet originating from the curvature of the base flow, so there is basically no net Stokeslet in the base flow; consequently, no Saffman force acts on the sphere.<sup>32</sup> The Saffman force is more relevant in the case of non-neutrally buoyant particles in a vertical flow, or an additional outer force (electrical or magnetic)<sup>35,36</sup> acting on the particle to lag or lead the fluid flow, creating an obvious net Stokeslet flow field. In this situation, the Saffman force will direct to the channel centreline when particles lag the flow, or direct toward the channel walls when particles lead the flow.

## 2.5 Wall-induced lift force

In the previous section, we mainly talk about the first effect of walls. The existence of a wall creates a velocity

gradient (shear rate) of fluid and possibly causes the rotation of spherical particles due to the shear. Thus, transverse Magnus force and Saffman force may act on the particles to migrate particles laterally. In addition, the second effect of walls is the change of the flow field around a particle in the presence of the walls. The net force on a particle near the wall differs from that of a particle in an unbounded flow. In order to eliminate the effects of shear rate to the lateral lift force, one possible scheme is investigating the motion of particles near a wall in a stagnant fluid.

In general, the effect of a wall on the motion of immersed objects is to retard the motion of the object in both parallel and perpendicular directions, as well as exerting a transverse migration motion. Two distinct interactions between an immersed object and a wall exist: (i) the motion of the immersed object is primarily influenced by a single wall on one side of the object. Any other walls are too far from the immersed object to influence significantly its motion. In this case, the main effects of the wall are decelerating the particle and driving the immersed object away from the wall (Fig. 1(c)). It applies to the situation where the characteristic dimension of the immersed particle is much less than the dimension of the flow channel. (ii) The immersed object is surrounded by the boundaries (walls) of the flow domain. Thus, the boundaries decelerate significantly the motion of the object. It happens if the characteristic dimension of the immersed particle is of the order of the dimension of the flow channel, such as small bubbles moving in capillaries, and the surrounding walls will constrain the motion of immersed particles.<sup>30</sup>

First, we discuss the situation where the dimension of the particles is much smaller than that of the channel. The particles are primarily influenced by a single wall. The direction of the particle motion can be perpendicular or parallel to the walls. When the immersed sphere moves perpendicularly to a boundary, the effect of the boundary will retard the motion of the particle, which is equivalent to the increase in the drag coefficient. Brenner<sup>37</sup> derived a first-order correction for the drag coefficient of a small sphere in the creeping flow moving towards a solid wall.

$$f_a = \frac{16\mu v_t}{a} f \quad (14)$$

$$f = \sinh \theta_w \sum_{n=1}^{\infty} \frac{n(n+1)}{(2n-1)(2n+3)} \times \left[ \frac{2\sinh[(2n+1)\theta_w + (2n+1)\sinh(2\theta_w)]}{4\sinh^2[(n+0.5)\theta_w] - (2n-1)^2 \sinh^2(\theta_w)} - 1 \right] \quad (15)$$

where  $\theta_w = \cosh^{-1}(2l_w/a)$  is a function of the ratio of the distance from the sphere centre to the wall to the particle diameter,  $l_w$  is the distance of the sphere centre to the channel

wall (Fig. 1(c)). Eqn (15) indicates that the hydrodynamic force on the particle increases significantly when the particle approaches the wall.

When the immersed sphere moves parallel to the boundary, a transverse lift force repels the particle away from the wall. Given the dimensionless distance  $d^* \ll 1$ , where  $d^* = \rho_f l_w v_s / \mu$ , the lateral migration velocity can be expressed as:<sup>38,39</sup>

$$v_z = \frac{3}{64} \text{Re}_s v_s \left\{ 1 - \frac{11}{32} d^{*2} + \dots \right\} \quad (16)$$

where  $v_s$  is the sedimentation velocity of the sphere in a quiescent fluid and  $\text{Re}_s$  is a Reynolds number defined by the sedimentation velocity and particle diameter, expressed as  $\text{Re}_s = \rho_f a v_s / \mu$ . Considering the implied condition of  $d^* \ll 1$ , it can be further simplified as:

$$v_z = \frac{3}{64} \text{Re}_s v_s \quad (17)$$

Eqn (17) indicates that the migration velocity of a sphere is constant when it is in the vicinity of the wall. This expression was experimentally validated by the data of Cherukat and McLaughlin<sup>40</sup> up to  $\text{Re}_s = 3.0$ .

In addition, when  $d^* \gg 1$ , the migration velocity then becomes:<sup>39</sup>

$$v_z = \frac{3}{16} \text{Re}_s v_s (d^{*-2} + 2.21901 d^{*-5/2} + \dots) \quad (18)$$

It indicates that for large values of  $d^*$  (large distance between sphere and wall or large sedimentation velocity of sphere), the migration velocity decreases continuously and tends to zero as  $d^* \rightarrow \infty$ .

In addition to the lateral lift force that repels a particle away from the wall, the effect of the boundary will also retard the sedimentation motion of the particle, corresponding to an increased drag force. The drag force experienced by a sphere settling down in the neighbourhood of a plane wall

$$\left( \frac{a}{2l_w} \ll 1 \ll \frac{1}{\text{Re}_s} \right) \text{ is:}^{39}$$

$$F_d = 3\pi\mu a v_s \left( 1 + \frac{3}{8} \text{Re}_s + \frac{9}{32} \frac{a}{l_w} + \dots \right) \quad (19)$$

At a relatively large distance  $\left( \frac{a}{2l_w} \ll \frac{1}{\text{Re}_s} \ll 1 \right)$ , the drag force is expressed as:<sup>39</sup>

$$F_d = 3\pi\mu v_s \left\{ 1 + \frac{3}{8} \text{Re}_s - 0.095 \frac{a}{l_w} \left( \frac{1}{\text{Re}_s} \right)^{3/2} + \dots \right\} \quad (20)$$

In a bounded flow, when the characteristic dimension of the sphere is of the same order of magnitude as the size of the flow channel, the surrounding boundaries provide a physical constraint to the flow, and in general, the immersed objects move close to the centreline of the channel. In order to prevent channel from being blocked, the blockage ratio  $\delta$  which is the ratio of particle diameter to channel diameter should be less than 1. Besides, the boundaries decelerate significantly the motion of the object. A wall drag multiplier of a rigid sphere moving in a cylindrical tube was derived and expressed as:<sup>30</sup>

$$K_{\text{wall}} = \frac{F_D}{3\pi a \mu v_s} = \left[ 1 - 2.0144\delta + 2.0888\delta^3 - 6.948\delta^5 - 1.372\delta^6 + \dots \right]^{-1} \quad (21)$$

In summary, the effects of walls on the motion of immersed spheres in a tube are to decelerate the motion of the sphere and repel particles to the centreline of the channel.

## 2.6 Shear gradient lift force

As discussed above, the particle will lag the flow due to the effects of the wall. If the curvature of the undisturbed fluid velocity profile is zero, it becomes a simple shear flow (Fig. 1(b)). Then the pressure will be higher on the left, pushing particles to the centreline of the channel. However, in the Poiseuille flow, the Stokeslet generated by the lag of the particle relative to the shear flow (slip-shear) may be balanced by an opposite Stokeslet originating from the curvature of the base flow. Furthermore, the curvature of the fluid velocity profile can even reverse this trend. Fig. 1(d) clearly shows that the magnitude of the relative velocity of fluid to particle is much higher on the left side of the particle than that on the right side due to the parabolic nature of the velocity profile, and it overwhelms the asymmetry caused by lag velocity. Similar to Saffman force, the dissymmetry of relative velocity causes a low pressure on the left/wall side, generating a shear gradient lift force that is opposite to the Saffman force. The shear-gradient lift force leads particles migrating toward the walls until the wall lift force repels and balances it.<sup>32,33</sup>

## 2.7 Net inertial lift force

For a neutrally buoyant rigid sphere flowing in a straight wall-bounded Poiseuille flow, besides a viscous drag force along the axis, there are four lateral forces acting on the sphere: Magnus force due to slip-rotation, Saffman force due to slip-shear, wall lift force due to the disturbance of the flow field around particles from the wall, and shear gradient lift force due to the curvature of the undisturbed fluid velocity profile. Among them, Magnus force and Saffman force are often very small and negligible. Shear gradient lift force, directing particles toward the channel walls, and wall lift force, repulsing particles toward the channel centreline, are commonly recognised as the dominant effects for the lateral migration of the particle.<sup>35</sup> The balance of shear gradient lift force and wall lift force creates several equilibrium positions

halfway between the channel walls and the centreline, and this theory can explain the observation of Segre and Silberberg reasonably<sup>12,13</sup> (Fig. 2(a)). It should be noted that such a breakdown is rather unconventional, since an unbounded parabolic velocity profile cannot be realized in practice, but permits the separation of the effects due to the curvature of the undisturbed velocity profile and the wall-induced disturbance.<sup>17</sup>

Through the method of matched asymptotic expansions, Asmolov<sup>17</sup> derived an analytical expression of the net inertial lift force acting on a small rigid sphere ( $a/H \ll 1$ ) in a Poiseuille flow:

$$F_L = f_L \rho_f U^2 a^4 \quad (22)$$

The force can be further simplified as:

$$F_L = f_L \rho_f U^2 a^4 / H^2 \quad (23)$$

The hydraulic diameter  $H$  is defined as  $H = D$  for a circular channel ( $D$  is the diameter of the circular cross section) or  $H = 2wh/(w + h)$  for a rectangular channel ( $w$  and  $h$  correspond

to the width and height of the rectangular cross section, respectively). The lift coefficient  $f_L$  is a function of the particle lateral position  $x$  and channel Reynolds number  $Re$ ,<sup>17,41</sup> Fig. 2(b). The lateral position  $x_{eq}$  where  $f_L = 0$  corresponds to the inertial equilibrium position. It should be noted that the channel centreline  $x = 0$  is not a stable equilibrium position, since a little deflection from the centreline will never return the particles back. It also has been found that  $f_L$  decreases with increasing  $Re$  (or  $U_f$ ), suggesting that inertial lift force scales less strongly than  $U_f^2$ .<sup>4</sup> Recently, Zhou and Papautsky<sup>42</sup> derived a scaling for the lift coefficient based on their experimental results:  $f_L \propto \frac{H^2}{a^2 \sqrt{Re}}$ . Although  $f_L$  varies with Reynolds number, at  $Re < 100$  that is typical for most microfluidic applications the lift coefficient remains relatively constant and can be approximated averagely as  $f_L = 0.5$ .<sup>43</sup>

For a finite-size particle ( $0.05 \leq a/H \leq 0.2$ ), the particle would cause disturbance to the main channel flow. Di Carlo *et al.*<sup>44</sup> calculated the inertial lift forces through finite element simulation, taking into account the finite-size effects of the suspended particles. The net force was scaled near the

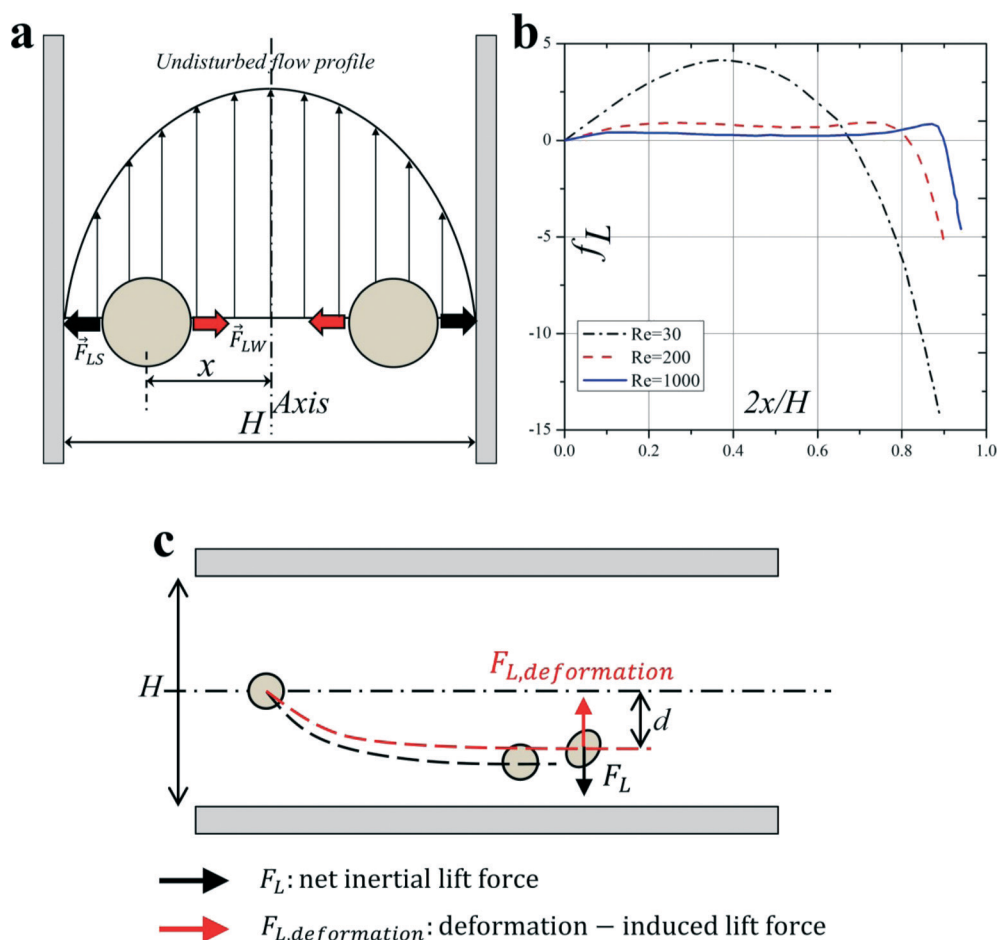


Fig. 2 (a) Balance of shear gradient lift force and wall lift force results in the inertial equilibrium positions in a Poiseuille flow. (b) The net lift coefficient is a function of the particle lateral position  $x$  and Reynolds number  $Re$ .<sup>22</sup> (c) Deformability-induced lift force directs to the channel centreline and shifts inertial equilibrium positions closer to the channel centre compared with the rigid spherical particles.<sup>45</sup>

channel centre and channel wall, respectively. Near the channel centre, where the effects of the wall are weak, the lift force scales as  $F_L \propto \rho_f U_f^2 a^4 / H^2$ , while near the channel wall, wall effects dominate, and it scales as  $F_L \propto \rho_f U_f^2 a^6 / H^4$ .

## 2.8 Deformability-induced lift force

Although solid rigid particles can be used as a simple model in the study of the hydrodynamic behaviour of particles in a microchannel, the practical bio-particles such as cells and vesicles are not rigid but deformable. The deformability will induce additional lift forces on the particles. The deformability-induced lift force is perpendicular to the main streamline, and it is believed to be the effects of shape-change of the particle and nonlinearities caused by the matching of velocities and stresses at the deformable particle interface.<sup>35</sup> Three dimensionless parameters can be used to characterize the relative deformation of a droplet: i) Weber number,  $We = \frac{\rho_f U^2 a}{\sigma}$  (inertial stress vs. surface tension),

where  $\sigma$  is the surface tension; ii) capillary number,  $Ca = \frac{\mu U a}{\sigma h}$  (viscous stress vs. surface tension); and iii) viscosity ratio,  $\lambda_d = \mu_d / \mu$ ; here  $\mu_d$  is the dynamic viscosity of fluid inside the droplet.<sup>35</sup>

Chan and Leal derived an analytical expression for deformability-induced lift force, given the condition that the drop or bubble is not too close to the walls:<sup>46,47</sup>

$$F_{L,\text{deformation}} = \mu U a \left( \frac{a}{H} \right)^2 \frac{d}{H} f(\lambda_d) \quad (24)$$

$$f(\lambda_d) = \frac{16\pi}{(\lambda_d + 1)^3} \left[ \frac{11\lambda_d + 10}{140} (3\lambda_d^3 - \lambda_d + 8) + \frac{3}{14} \frac{19\lambda_d + 16}{3\lambda_d + 2} (2\lambda_d^2 - \lambda_d - 1) \right] \quad (25)$$

where  $d$  is the distance between the drop and the centre of the channel. Furthermore, the condition of  $\lambda_d < 1$  or  $\lambda_d > 10$  was specified for the deformability-induced lift force directing towards the centre of the channel.<sup>47</sup>

The experimental measurement of the inertial lift force by Di Carlo *et al.*<sup>44</sup> was used to extract an equation for inertial lift force near the channel centre where  $d/H < 0.1$ . The negative sign indicates that this force,  $F_{L,\text{inertial}}$ , is directed towards the walls.

$$F_{L,\text{inertial}}^{\text{center}} = -10R_p \mu U a \left( \frac{d}{H} \right) \quad (26)$$

When both drop deformation and inertial lift forces are small (for  $Ca < 0.01$  and  $R_p < 0.01$ ), Stan *et al.*<sup>46</sup> introduced an empirical formula for net lift force on drops or bubbles as:

$$F_{L,\text{empirical}} = C_L \mu U a \left( \frac{a}{H} \right)^3 \left( \frac{d}{H} \right) \quad (27)$$

Here lift coefficient  $C_L$  must be determined from experimental measurements for each pair of the continuous and dispersed phases, and  $C_L \sim 31.25$  can be used for the order-of-magnitude estimate.<sup>46</sup>

Deformability-induced lift force can be used to separate and enrich malaria-infected red blood cells (iRBCs) from normal healthy RBCs (hRBCs) for the diagnosis of malaria. The parasite releases proteins that trigger the cross-linking of the spectrin network in the iRBC's phospholipid bilayer membrane, thus increasing the rigidity of the iRBCs. Normal hRBCs are more deformable than iRBCs, migrating towards the centre of the channel. Due to the massive hydrodynamic interactions and mechanical collisions between the RBCs in high haematocrit (Hct) blood, stiffer malaria iRBCs are displaced towards the sidewalls and can be depleted and enriched by bifurcated outlets.<sup>48</sup>

In inertial microfluidics, Hur *et al.*<sup>45</sup> found that centre-directed deformability-induced lift force shifts inertial equilibrium positions a little closer to the channel centreline than that of rigid particles (Fig. 2(c)). By the combination of size and deformability, circulating tumor cells (CTCs) with more deformability than the cells from the same organ have been demonstrated to be separated and enriched from peripheral blood.<sup>45</sup>

Besides particle deformability, the shape of particles<sup>49</sup> and the properties of the medium<sup>50</sup> also impact the inertial migration and equilibrium positions, which will not be discussed here. A summary of particle kinetics in inertial microfluidics is shown in Fig. 3.

## 3 The recent progress of inertial microfluidics

According to the structure of the functional microchannel, the reported inertial microfluidic devices can be categorised according to their channel structure as (i) straight channels, (ii) spiral channels, (iii) straight channels with pillar arrays or expansion-contraction arrays, and (iv) serpentine channels. In this chapter, we review the current progress of inertial microfluidics, including the phenomenon and possible explanation of inertial migration in different structured microchannels as well as their application in biomedicine and disease diagnosis. The characteristics of inertial forces in different structured channels are summarized in Table S1.<sup>†</sup>

### 3.1 Straight channel

In a straight channel with a circular cross section, the randomly distributed particles migrate laterally to a narrow annulus at about 0.6 times of the channel radii from the axis,<sup>12,22</sup> as depicted in Fig. 4(a). However, in a straight channel with a rectangular cross section, which is the most widely used structure due to the limitation of microfabrication, the

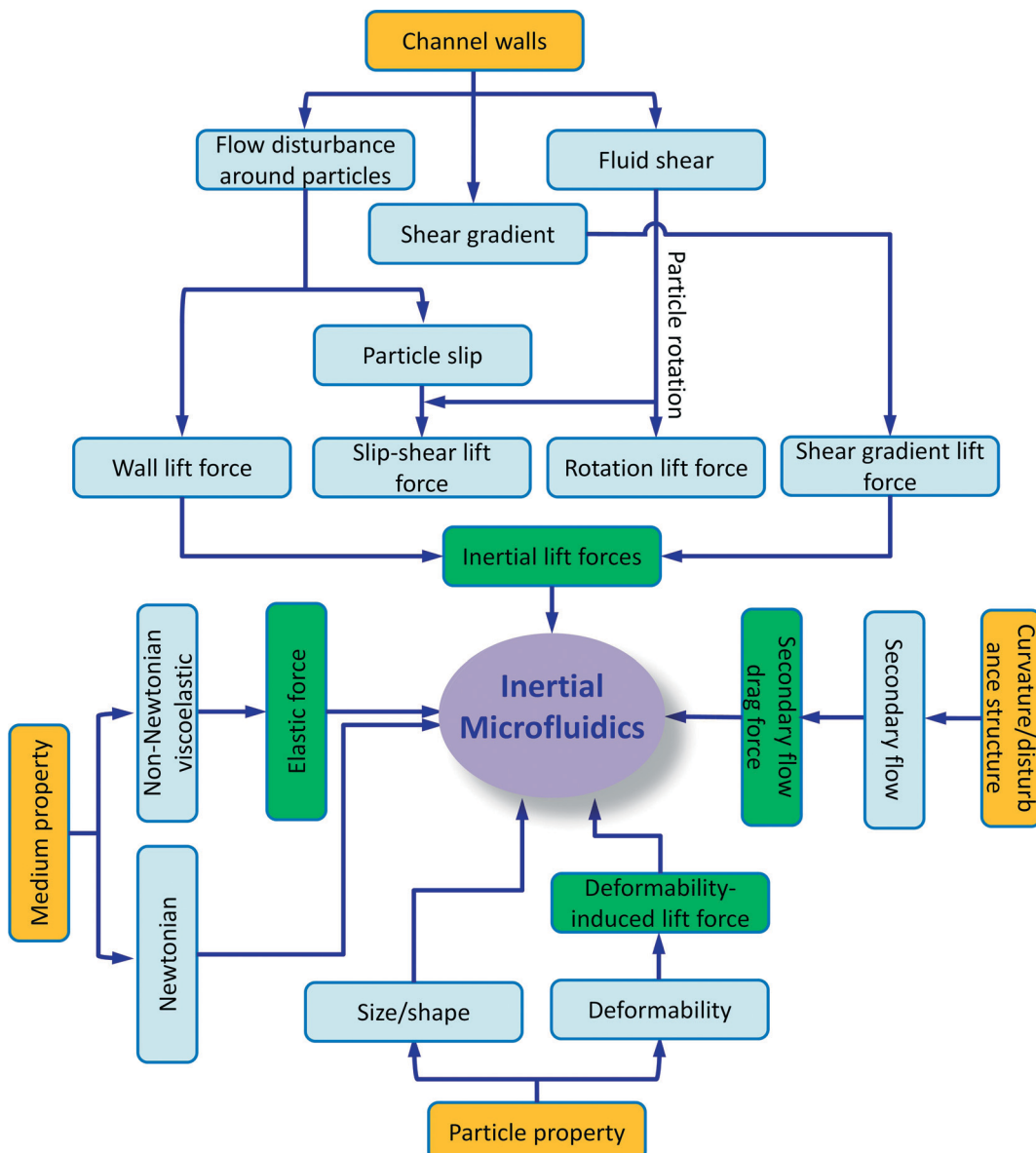


**Fig. 3** Outline of particle kinetics in inertial microfluidics. There are four aspects impacting inertial focusing in inertial microfluidic systems: channel walls, channel curvature or disturbance structure, particle and medium property. Channel walls create wall lift force, shear gradient lift force, slip-shear lift force and rotation lift force on particles, while front two lift forces are widely recognised as responsible for inertial migration phenomenon. Channel curvature or disturbance structure generates secondary flow, which assists the inertial focusing process and modifies final inertial focusing positions. Besides, the properties of particle (e.g. size, shape and deformability) and medium (Newtonian, viscoelastic) also influence the final inertial focusing positions.

situation becomes more complex. In a square straight channel ( $AR = \text{height}/\text{width} = 1$ ), particles normally focus to four equilibrium positions,<sup>51</sup> facing the centre of each wall (Fig. 4(b)). Additionally, a further reduction to two equilibrium positions happens in a low aspect ratio ( $AR \approx 0.5$ ) channel, and particles focus at the centre about  $0.2H$  away from the long walls (see Fig. 4(c)).<sup>42,52,53</sup> One explanation about this equilibrium position's reduction was given by Zhou and Papautsky<sup>42</sup> by a two-stage migration model which is illustrated in Fig. 4(c).

In a straight channel, the particles' lateral migration velocity ( $U_L$ ) and the minimum channel length ( $L_{\min}$ ), which is the minimum length that is required for particles to migrate to their

inertial equilibrium positions, can be derived by balancing the net inertial lift force with Stokes drag (see Fig. 4(d)):<sup>41</sup>

$$F_{\text{stks}} = 3\pi\mu a U_L \quad (28)$$

$$U_L = \frac{F_L}{3\pi\mu a} = \frac{\rho_f U^2 a^3}{6\pi\mu H^2} \quad (29)$$

$$L_{\min} \approx \frac{H}{2U_L} \times U = \frac{3\pi\mu H^3}{\rho_f U a^3} \quad (30)$$

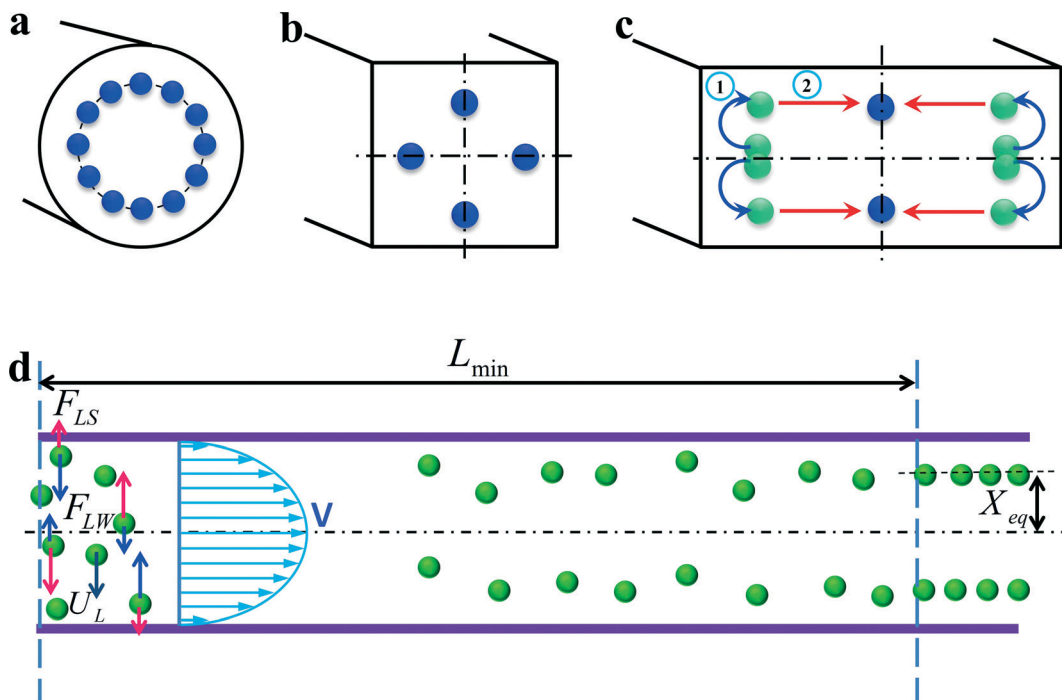


**Fig. 4** Inertial equilibrium positions in a straight channel with different cross sections: (a) circular cross section; (b) square cross section, and (c) rectangular cross section with low aspect ratio ( $\approx 0.5$ ). Illustration of two-stage migration model proposed by Zhou and Papautsky.<sup>42</sup> (d) The lateral migration speed  $U_L$  and minimum channel length for particle focusing  $L_{\min}$ .

Two dimensionless Reynolds numbers can characterize the lateral migration of particles in a straight channel: channel Reynolds number  $Re$  describing the ratio between inertial force and viscous force of fluid in a flow, and particle Reynolds number  $R_p$  additionally considering the size ratio of particle to channel.

$$R_p = Re \frac{a^2}{H^2} = \frac{\rho_f U a^2}{\mu H} \quad (31)$$

When  $R_p \ll 1$ , particles are subjected to the dominant viscous drag to follow fluid streamlines. However, on increasing  $R_p$  to the order of 1, inertial lift forces become dominant and lateral migration of particles across the fluid streamlines becomes obvious.<sup>43</sup>

Although a straight channel is often employed as a basic model to investigate the fundamental mechanism of inertial migration due to its simplicity,<sup>18,42,44,54–56</sup> this channel type has been utilized for a variety of applications. Hur *et al.*<sup>57</sup> demonstrated the purification of adrenal cortical progenitor from digestions of murine adrenal glands utilizing hydrodynamic inertial lift forces in a straight micro-channel with high aspect ratio (Fig. 5(a)). The inertial focusing position depends on the cell size, where larger cells are closer to the channel centre, and smaller cells are closer to the channel walls. Differentially focused cells can be collected at designated outlets based on apparent diameter.

Mach and Di Carlo<sup>58</sup> reported a massively parallelized microfluidic device that passively separates pathogenic bacteria from diluted blood (Fig. 5(b)). The device consists of 40

single straight micro-channels placed as a radial array. Each channel consists of three segments with different cross sections, which uses a unique differential transit time by size-dependent inertial lift forces to obtain cell separation. The authors demonstrated that more than 80% pathogenic bacteria can be removed after passing two times through the same system. The parallel device can process 240 mL h<sup>-1</sup> with an extremely high throughput of 400 million cells per minute. Later, Zhou and colleagues<sup>59</sup> utilized a modified design on size and length for their cascaded straight channels, as shown in Fig. 5(c). The separation concept is based on the theory of two-stage inertial migration, which permits precise prediction of particle or cell position within the micro-channel. Randomly distributed particles first flow through a high AR channel (segment I) where particles are focused at half of the channel height near two sidewalls. Then the channel expands into a low AR channel (segment III), which modifies equilibrium positions to the centres of the top and bottom walls. Since larger particles have a much higher migration velocity, they reach the relocated points very quickly. In contrast, lift forces on smaller particles are too weak to alter their lateral position. This effect enables a separation of particles by size. After this modification, much higher separation efficiency (~99%) and purity (~90%) were achieved in their work.

Manual concentration, staining and washing procedures for cellular samples are routinely conducted by cytopathologists as a means of diagnosing malignancies and other diseases. However, current approaches for chemical treatments of cells and chemical reactions typically operate on slow time scales (~seconds to minutes), limiting the realm

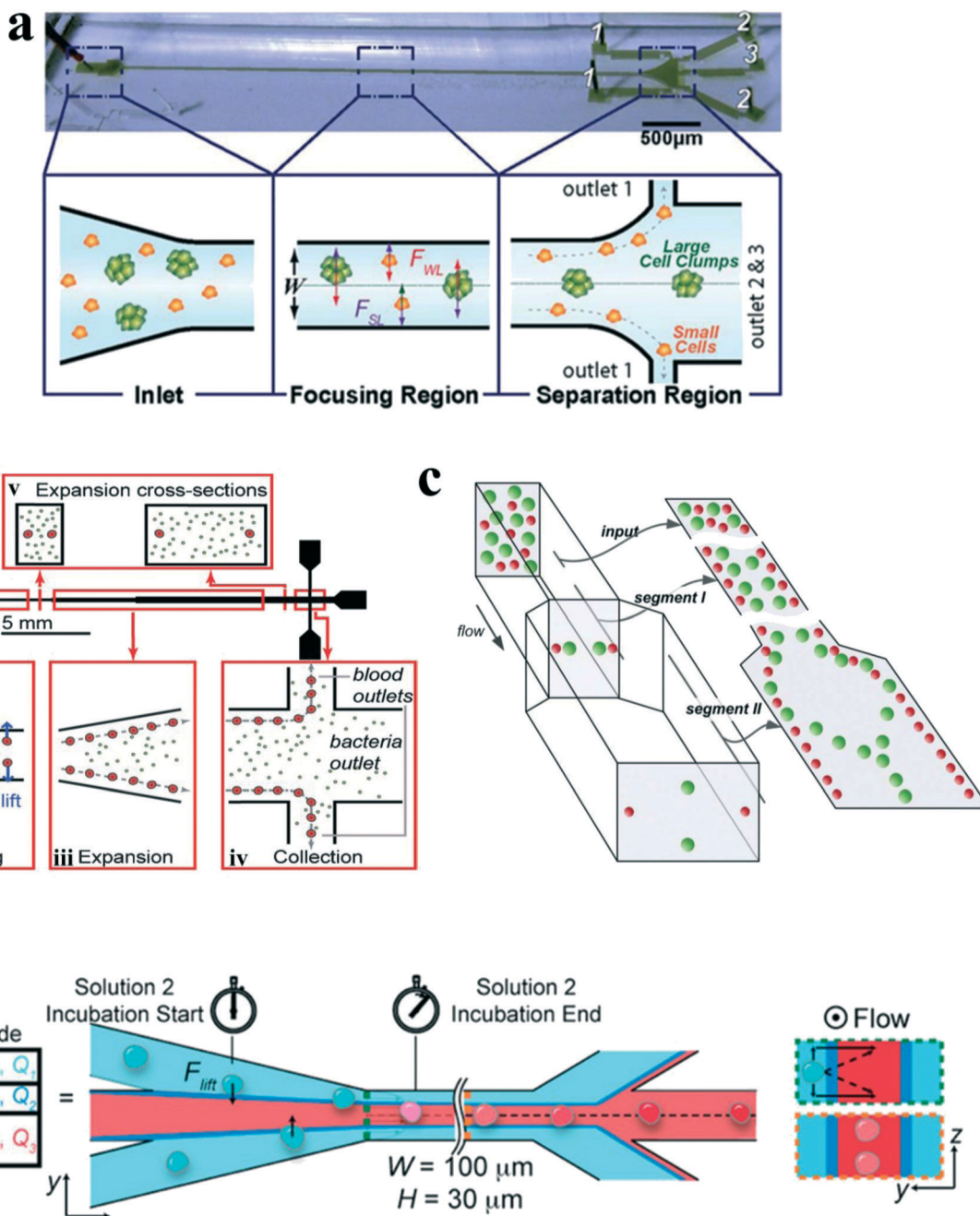


**Fig. 5** (a) Label free isolation of adrenal cortical progenitor cells by size-based differential inertial focusing in a straight channel. Reproduced from ref. 57, an open-access article. (b) Separation of pathogenic bacteria from diluted blood in a series-connected straight channel which utilizes a unique differential transit time by size-dependent inertial lift forces. Reproduced from ref. 58 with permission from John Wiley and Sons. (c) Complete separation of particles in a cascaded channel with two straight segments with different aspect ratios (ARs). Reproduced from ref. 59 with permission from the Royal Society of Chemistry. (d) Rapid inertial solution exchange in a straight channel for controlled interaction of reagents with cells and particles. Reproduced from ref. 60 with permission from the American Chemical Society. Copyright 2014.

of fast molecular events. Inertial lateral migration has been subtly employed as a helpful tool to mediate millisecond reaction time around particles and cells,<sup>60</sup> as shown in Fig. 5(d). The main transfer channel is designed with a low aspect ratio, so particles will migrate to the lateral centre of a channel. The channel has three inlets. The particle suspension is infused from the two side inlets, while the reagent is pumped in from the central inlet. Lateral migration of

particles from the original medium to the middle stream initiates the contact of particles/cells with the chemical reagent, and the duration of particles within the middle stream mediates the reaction time. The proposed microfluidic system can perform several functions in the sample preparation for cytopathology that (i) automates colorimetric staining on-chip, (ii) images cells in flow, and (iii) provides additional quantitative analyses of captured images to aid cytopathologists.<sup>61</sup> In

addition, ordering particles along a specific stream within a simple straight microchannel could also be integrated with an optical detector to form an on-chip flow cytometer system. In another study, Hur *et al.*<sup>62</sup> proposed an extremely high-throughput on-chip imaging flow cytometry consisting of 256 high-aspect ratio parallel straight channels and a high-speed optical camera, promising interrogation rates up to 1 million cells per second.

In general, a straight channel has the advantage of simplicity and ease of operation. Therefore, the mechanism of inertial migration phenomenon in a straight channel is relatively clear and has already been studied extensively. However, since  $F_L \propto H^{-2}$ , the sizes of channel cross sections are normally restricted to provide enough lateral lift forces. In addition, the channel is relatively long, which would add up the flow resistance and lead to a large device footprint. In the following section, we will see that the introduction of a secondary flow by channel curvature or obstacle structure will not only aid the inertial migration progress but also modify the final equilibrium positions. However, its mechanism becomes more complex and demands a more rigorous explanation.

### 3.2 Spiral channel

The introduction of channel curvature along a single constant direction forms a spiral channel. When fluid flows through a curved channel, a secondary flow arises due to the

velocity mismatch in the downstream direction between fluid in the central and near-wall regions. The fluid elements near the channel centreline have a larger inertia and would tend to flow outward around a curve due to the centrifugal effect, creating a pressure gradient in the radial direction within the channel. In a fully bounded channel, due to the centrifugal pressure gradient, relatively stagnant fluid near the walls recirculates inward, finally forming two symmetric circulating vortices<sup>4</sup> (Fig. 6(a)). The parameters that influence the distribution and strength of the secondary flow in a curved channel include Dean number  $K$ , Reynolds number  $Re$  and aspect ratio  $AR$  of the channel. Dean number  $K$  is a function of Reynolds number  $Re$ , the hydraulic diameter for the rectangular channel  $H$  and the radius of curvature  $R$ .<sup>23</sup>

$$K = (H/2R)^{1/2} Re \quad (32)$$

Following Squires and Quake,<sup>63</sup> the secondary flow velocity scales as

$$U_D \sim K^2 \mu / (\rho H) \quad (33)$$

Furthermore, the magnitude of the secondary flow  $U_D$  can be approximated as:<sup>64,65</sup>

$$U_D = 1.8 \times 10^{-4} \times K^{1.63} \quad (34)$$

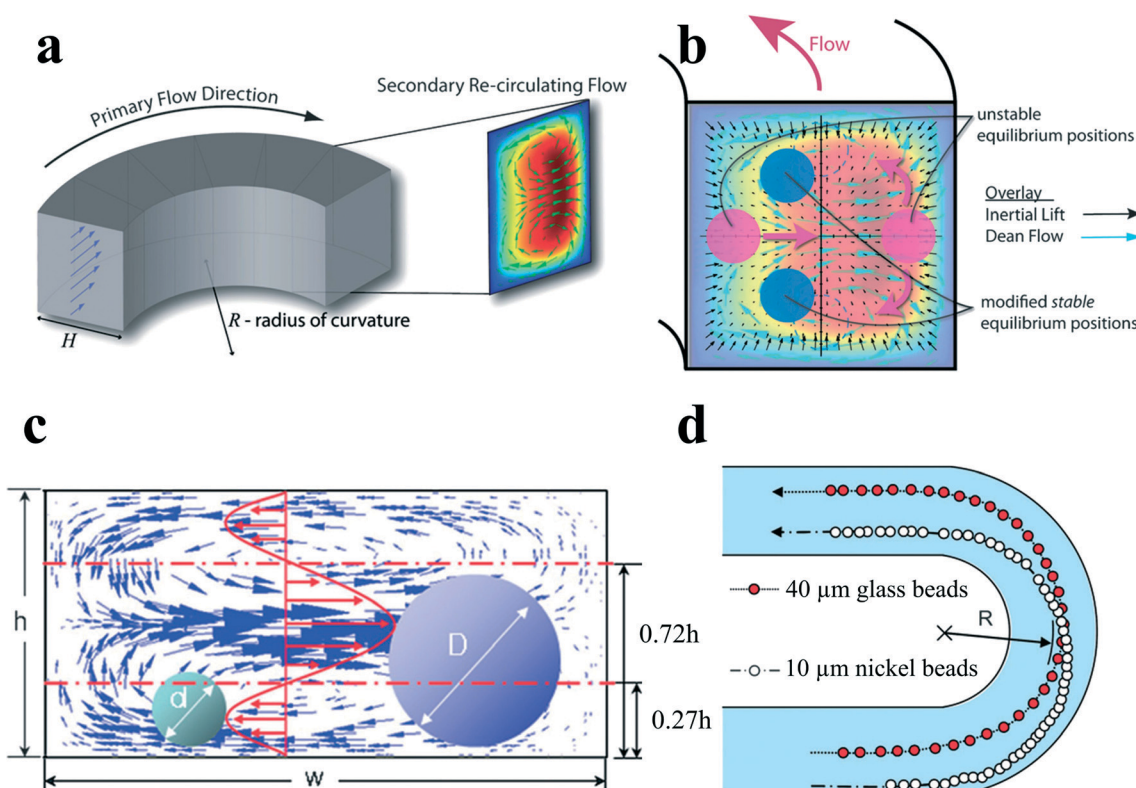


Fig. 6 (a) Dean flow with two counter-rotating vortices is created in curved channels. Reproduced from ref. 4 with permission from the Royal Society of Chemistry. (b) Superposition of inertial lift force and Dean flow in a curved channel modifies the number and position of the inertial equilibrium positions. Reproduced from ref. 4 with permission from the Royal Society of Chemistry. (c and d) Size-based separation by the different directions of secondary flow drag force exerted by the velocity distribution. Reproduced from ref. 66 with permission from the Royal Society of Chemistry.

In addition, the ratio of channel dimension to radius of curvature  $\delta = H/2R$ , Dean number  $K$  as well as the aspect ratio AR have important effects on secondary flow distribution.<sup>23</sup>

Particles flowing in a curved channel with finite inertia will experience both inertial lift forces and secondary flow drag. In most cases, the density of the particle is very close to that of the fluid, so the effect of particle centrifugal force around channel curvatures is negligible. When the channel curvature is along a single direction, the curved channel is a spiral channel, and the direction of secondary flow within each cross section is constant, although there might be a little variation in its magnitude due to the change in channel curvature. By a first-order approximation, one can make an assumption that the effects of inertial migration and secondary flow act in superposition on particles in spiral channels (Fig. 6(b)). A particle held stationary at inertial equilibrium positions experiences a secondary flow drag whose magnitude is directly proportional to the local secondary flow velocity.<sup>4</sup> This secondary flow drag force acts to entrain particles within the streamline of symmetrically rotating vortices, which is primarily an effect of mixing. In contrast, inertial lift forces tend to hold particles at specific equilibrium positions within the channel cross section. Therefore, the order of magnitude scaling between inertial lift forces and Dean drag  $R_f = \alpha^3 R/H^3$  determines the final behaviour of the suspended particles. This dimensionless parameter is useful for the prediction of particle behaviour in curved channels.

At limiting conditions where (i)  $R_f \rightarrow 0$ , Dean drag force dominates the behaviour of particles; particle streams neglect inertial equilibrium positions and remain entrained within the secondary flow streamlines, and (ii)  $R_f \rightarrow \infty$ , inertial lift force, is dominant; particles migrate to the inertial equilibrium positions independent of the secondary flow.<sup>4</sup> For most cases, in the intermediate range of  $R_f$ , inertial equilibrium positions will be modified by the secondary flow (Fig. 6(b)), leading to a very intriguing new focusing phenomenon. It has been noted that  $R_f$  is dependent on particle size so that two different-sized particles may experience different forces in the same curved channel. Therefore, it would be possible to separate particles by size in spiral channels.

Yoon *et al.*<sup>66</sup> proposed another kind of particle separation in a curved channel. In their work, the separation was achieved by the net effect of secondary flow velocity distribution rather than the theory of the balance between secondary flow drag and inertial lift forces. Larger particles with diameters larger than  $0.72h$  experience a net secondary flow drag directing outward to the channel curvature, while smaller particles with diameters less than  $0.27h$  experience a net secondary flow drag inward (Fig. 6(c) and (d)). Therefore, particles can be separated based on altered net direction of secondary flow drag on different-sized particles.

Spiral channels were investigated extensively for particle ordering and separation by Papautsky's group,<sup>57,68</sup> Go's group,<sup>66</sup> Jiang's group,<sup>69,70</sup> Han's group,<sup>71,72</sup> etc. Bhagat *et al.*<sup>64</sup> proposed a sheath-less, on-chip flow cytometry system based on the principle of Dean coupled inertial microfluidics

(Fig. 7(a)). The microfluidic flow cytometry system could provide a throughput of 2100 particles per second. Furthermore, Kemna *et al.*<sup>65</sup> reported an integrated microfluidic system that combines cell-ordering in a spiral channel with a droplet microfluidic generator. Cells were focused in three dimensions along a single particle chain and ordered with a precise longitudinal space (Fig. 7(b)). Single cell encapsulation was successfully demonstrated downstream with an efficiency of about 80%. Such a system is very promising in applications such as cell-based assays, drug screening and cell printing technologies.

Passive separation and sorting of particles/cells is one of the superior advantages for spiral microchannels, benefiting from the distinct size dependence characteristics of secondary flow and inertial lift forces. In another work, Bhagat and colleagues<sup>67</sup> demonstrated a complete separation of  $7.32\text{ }\mu\text{m}$  and  $1.9\text{ }\mu\text{m}$  polystyrene particles at a Dean number of 0.47 in a 5-loop spiral microchannel. Later, Kuntaegowdanahalli and co-workers<sup>68</sup> from the same group extended the separation capability of spiral channels. The authors demonstrated continuous separation of triplet polystyrene beads (10, 15 and 20  $\mu\text{m}$  in diameter) with an efficiency of 90% and a throughput of  $1 \times 10^6$  cells per min in a spiral channel (Fig. 7(c)). Furthermore, this separation ability was employed to separate different-staged cells for cell cycle synchronization, which is essential for studying cellular properties, biological processes and elucidating genetic regulatory mechanisms and events involved in each phase prior to cell division.<sup>73</sup>

Cancer, also known as a malignant tumour, is a group of diseases involving abnormal cell growth with the potential to invade or proliferate in other organs of the body. Metastases from primary tumours are the leading causes of death (~90%) for nonhematological cancers.<sup>74</sup> During the progression of metastasis, cancer cells escape from solid tumours and enter the bloodstream, becoming circulating tumour cells (CTCs), which hold a great potential to serve as important biomarkers for early diagnosis of cancer metastases as well as cancer prognosis and therapy monitoring. CTC analyses are considered as a real-time "liquid biopsy", which is much less invasive than the current method for cancer diagnosis requiring invasive biopsy followed by molecular analysis. However, CTCs are extremely rare, comprising only a few out of one billion haematological cells in blood, making their isolation and characterization an extreme technological challenge.

In an intriguing work, Hou *et al.*<sup>75</sup> employed a spiral channel to isolate CTCs from blood under the assistance of a sheath flow, and it achieved a recovery rate of more than 85%. This CTC isolation platform works in a label-free and clog-free continuous manner, significantly reducing the capturing costs and alteration of CTC morphology. In addition, a clinical validation with positive detection of CTCs from all the patients' blood samples was reported. Meanwhile, Sun and colleagues<sup>69,70</sup> reported a passive double spiral microfluidic device (Fig. 7(d)), which can separate and enrich tumour cells (MCF-7 and HeLa cells) from diluted whole

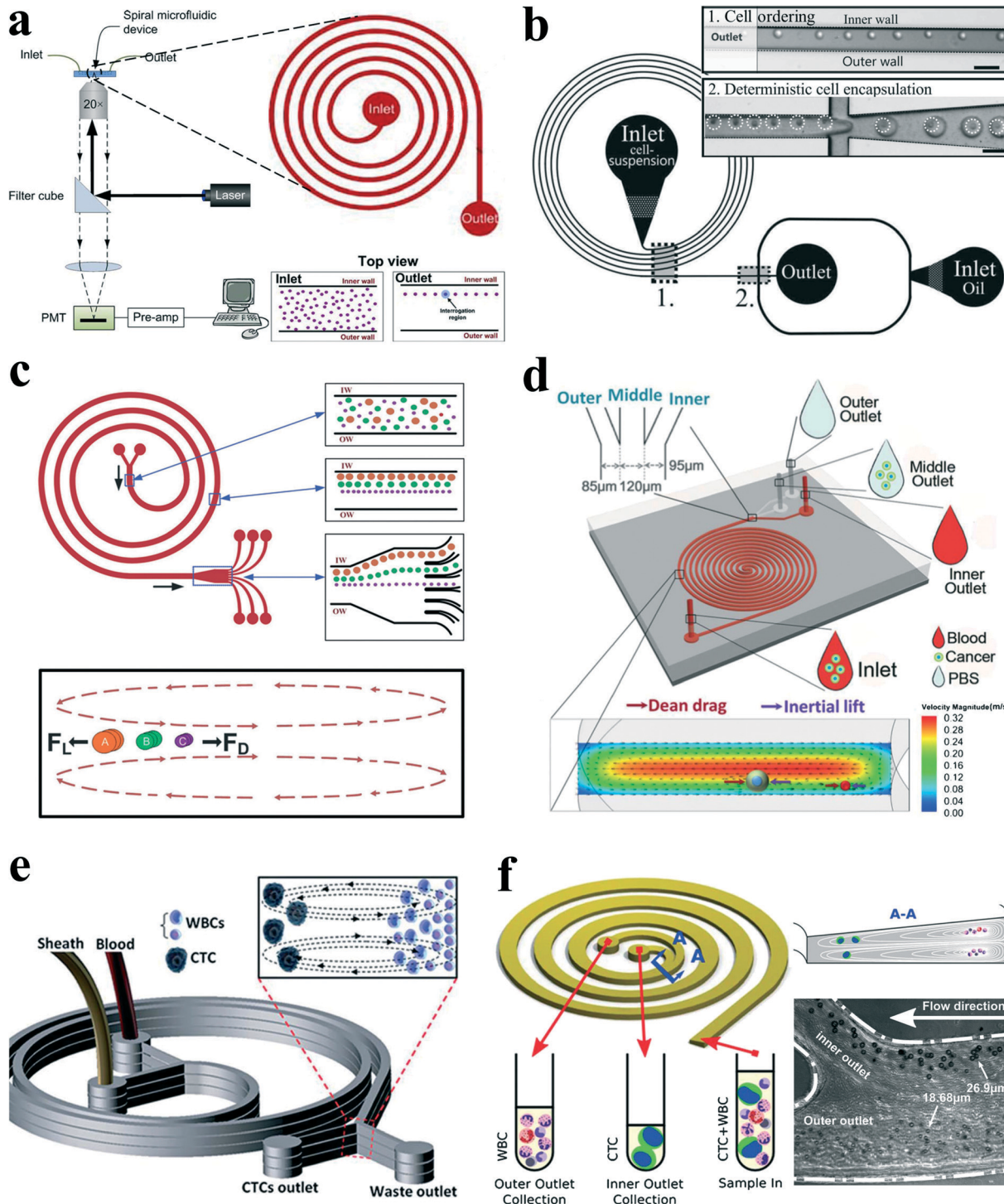


**Fig. 7** (a) Schematic of a microfluidic flow cytometry, in which a spiral channel is applied as a particle focuser to provide high-throughput sheathless 3-D focusing, followed by the downstream laser induced fluorescence setup for particle detection and counting. Reproduced from ref. 64 with kind permission from Springer Science & Business Media. (b) Single cell encapsulation by droplets in a spiral channel. The spiral channel promotes single cell stream ordering with a precise longitudinal spacing, and the downstream droplet generator encapsulates cells into the droplets. Reproduced from ref. 65 with permission from the Royal Society of Chemistry. (c) Continuous triplet-particle separation in a spiral channel. Reproduced from ref. 68 with permission from the Royal Society of Chemistry. (d) Double spiral microchannel for tumour cell separation and enrichment. Reproduced from ref. 69 with permission from the Royal Society of Chemistry. (e) A multiplexed microfluidic device stacked by three spiral channels for ultra-high throughput CTC capturing and enrichment.<sup>76,78</sup> (f) Ultra-fast, label-free enrichment of CTCs from blood samples by a spiral microfluidic device with a trapezoidal cross section. CTCs are focused near the inner wall due to the combination of inertial lift force and Dean drag force, while white blood cells and platelets are trapped inside the core of the Dean vortex closer to the outer wall.<sup>71</sup>

blood with a throughput of  $3.33 \times 10^7$  cells per min. Compared to the single spiral microchannel, the double spiral device was claimed to provide better focusing behaviour of small blood cells and improved separation efficiency. To further scale up the throughput of spiral channels, parallelization technology must be employed. Warkiani *et al.*<sup>76</sup> reported a multiplexed microfluidic device stacked by three spiral channels along vertical direction for ultra-high throughput CTC capturing and enrichment (Fig. 7(e)). The advantages of very fast processing speed (7.5 ml blood in less than 10 min) and the ability to collect more CTCs from larger blood volumes make it very promising for a range of potential genomic and transcriptomic applications.

Guan and co-workers<sup>77</sup> introduced a novel spiral micro-channel with a trapezoidal cross section and it showed a higher separation resolution than those with a rectangular cross section. Their study found that particle focusing in a spiral channel with a trapezoidal cross section is sensitive to particle size and flow rate and exhibits a sharp transition at a size-dependent critical flow rate. Wu *et al.*<sup>72</sup> applied this novel spiral channel for the separation of leukocytes from blood sample. At the outlet, the larger white blood cells focus near the inner walls, while smaller red blood cells are trapped at the core of the Dean vortex near the outer wall. An enhanced separation resolution and efficiency (>80%) was demonstrated. Later, isolating CTCs from blood samples of cancer patients was demonstrated by the same group using similar slanted spiral micro-channels<sup>71</sup> (Fig. 7(f)). The device has successfully isolated and recovered more than 80% of the tested cancer cell lines spiked in 7.5 ml blood within 8 min with high purity (400–680 WBCs per ml, ~4 log depletion of WBCs). In the initial clinical investigation, the trapezoid chip successfully isolated CTCs from 10 out of 10 (100%) patients with advanced stage metastatic breast and lung cancer (3–125 CTCs per ml), and it allowed extensive heterogeneity studies *via* immunostaining and DNA FISH analysis.

### 3.3 Straight channel with pillar arrays or expansion-contraction arrays

Besides curvature, the introduction of disturbance obstacles into straight channels will also induce convective secondary flow, which was first reported to enhance mixing effects by continuously splitting and redirecting fluid streams.<sup>24</sup> By patterning a contraction-expansion array on a single side of a straight channel, Park's group<sup>79</sup> successfully demonstrated three-dimensional single stream particle focusing under a sheath flow. At the entrance of the contraction region, the centrifugal forces induce a counter-rotating secondary flow, enveloping a sample flow with a sheath flow in three dimensions. Besides particle focusing, a series of particle separations in this kind of contraction-expansion array (CEA) channels were also reported by the same group, including separating polystyrene beads of 4  $\mu\text{m}$  and 10  $\mu\text{m}$  in diameter,<sup>53</sup> blood plasma from red blood cells<sup>80</sup> and cancer cells from whole blood<sup>81</sup> (Fig. 8(a)). The expansion-contraction

array induces Dean-like secondary rotating flows, working together with inertial lift forces on the suspended particles. Large particles or cells such as cancer cells are influenced dominantly by the inertial lift forces, migrating towards the contraction-expansion side, while small particles or cells (*e.g.* red blood cells and white blood cells) are dominated by Dean drag, shifting towards the opposite side. Finally, it enables a size-based particle/cell separation and enrichment.<sup>81</sup>

The contraction-expansion array can also be patterned on two sides of the channel. Park *et al.*<sup>82</sup> investigated particle inertial focusing in a straight channel patterned with symmetrical expansion-contraction arrays on both sides (multi-orifice microchannel) (Fig. 8(b)). This device works without any sheath flow. The ordered particle distribution can be achieved at central or side regions according to a particle Reynolds number  $R_p$ . Generally, particles are focused at two side positions with the  $R_p$  range of ~0.8 to 2.3 and at the centreline with the  $R_p$  range of 3.0 to 3.5. The mechanism of these focusing patterns relies on the combination of inertial lift force and momentum-change-induced inertial force generated in the contraction-expansion region. The trajectory mismatch between particles and fluid elements around the contraction-expansion region induces the lateral drift of the equilibrium position. The extent of this lateral drift is variable according to particle size and flow rate. In the Reynolds number range of 63 to 91, large polymer particles (~15  $\mu\text{m}$ ) were aligned at the centreline of the outlet, whereas small particles (~7  $\mu\text{m}$ ) remained along both sidewalls. Therefore, size-based separation of particles in this kind of multi-orifice channel is achieved and termed multiorifice flow fractionation (MOFF).<sup>83</sup> The MOFF has several advantages such as continuous, label-free, sheath-less, and non-intrusive with minimal power consumption. However, it is limited by the relatively low recovery yield. Although the recovery yield may be increased by adjusting parameters such as the Reynolds number to enhance central focusing, poor purity inevitably followed. Both high recovery yield and high purity cannot be warranted at the same time. Therefore, Sim *et al.*<sup>84</sup> presented a multi-stage multi-orifice flow fractionation (MS-MOFF), which is made by combining three multi-orifice segments, 3 inlets, 3 filters and 5 outlets. It could improve recovery and minimize loss of purity by collecting and re-separating non-selected particles from the previous separation. The final recovery rate was successfully increased from 73.2% to 88.7% without significant compromise on purity. By combining multi-orifice flow fractionation (MOFF) with dielectrophoresis (DEP) techniques, Moon *et al.*<sup>85</sup> successfully separated human breast cancer cells (MCF-7) from a spiked blood sample (Fig. 8(c)). The inertial separation by MOFF takes advantage of the high-throughput filtration of blood cells, and the serially connected DEP separator works as a precise post-processor to further enhance the separation efficiency and purity.

Diagnosis of malaria at the early stage of infection is challenging due to the difficulty in detecting the low abundance of parasites from blood. The polymerase chain reaction (PCR)

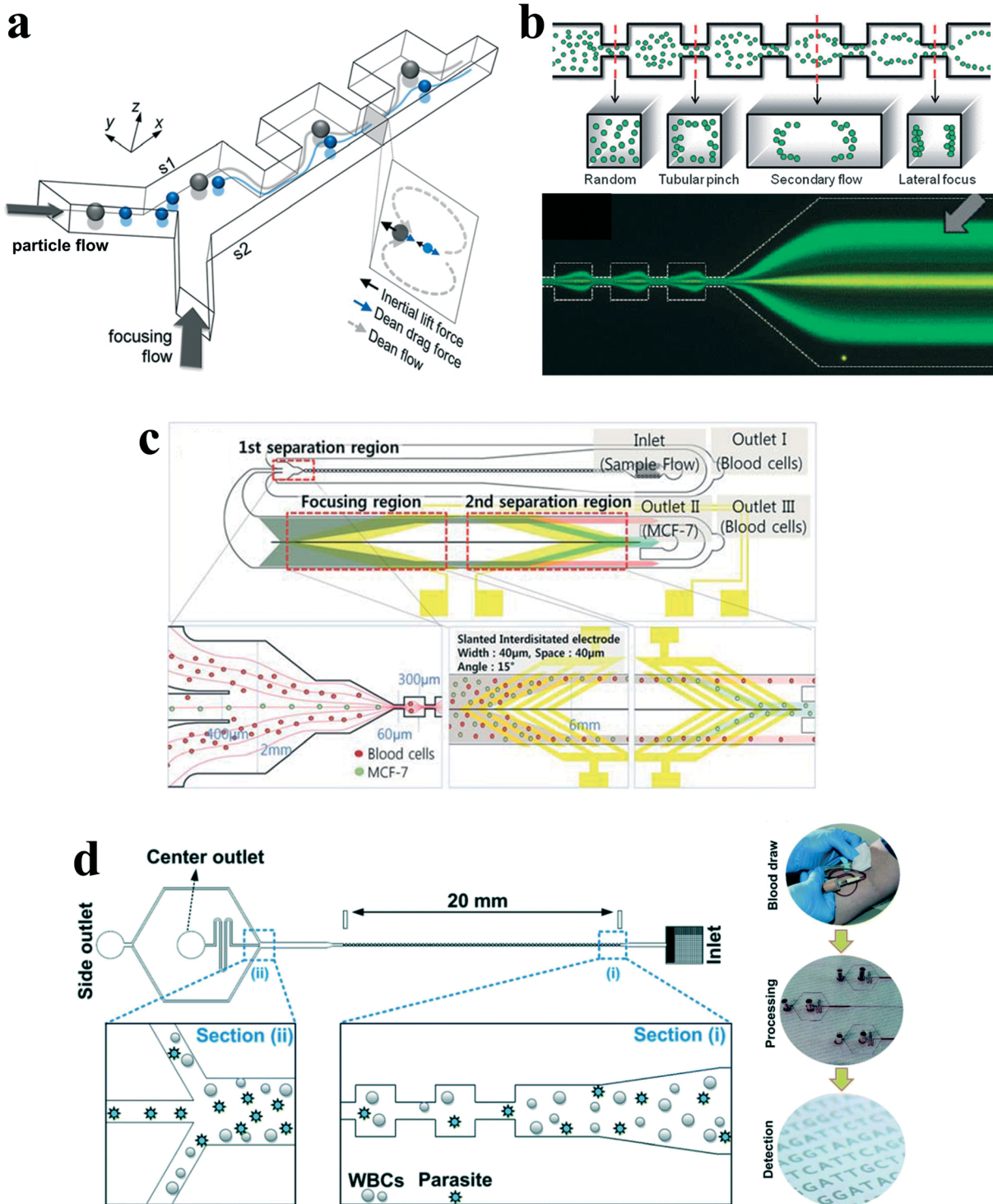


**Fig. 8** (a) Inertial separation of particles by size in a CEA channel under the assistance of a sheath flow. Reproduced from ref. 53 with permission from Elsevier. (b) Continuous inertial separation in a multi-orifice microchannel according to the size-dependent lateral migration termed as multiorifice flow fractionation. Reproduced from ref. 82 and 83 with permission from the Royal Society of Chemistry and American Chemical Society. Copyright 2009. (c) Continuous high-throughput separation of human breast cancer cells (MCF-7) from blood cells by a combination of multi-orifice flow fractionation (MOFF) and dielectrophoresis (DEP). Reproduced from ref. 85 with permission from the Royal Society of Chemistry. (d) Improved detection of malaria by the integration of inertial microfluidic processing and PCR detection.<sup>86</sup>

method can be especially useful to detect low parasitemia levels, but the efficiency is discounted by many factors, such as limited specificity of primers, presence of PCR inhibitors

in blood serum and DNA contamination from nucleated blood cells. Recently, Warkiani and co-workers<sup>86</sup> presented an improved detection method for malaria by the

combination of inertial microfluidic processing and PCR detection (Fig. 8(d)). In the symmetrical contraction–expansion channel, particles larger than 4  $\mu\text{m}$  such as WBCs were focused along the channel walls and isolated *via* the peripheral outlets. The malaria parasites, on the other hand, were unfocused and distributed in all the three outlets. Therefore, an enriched and purified blood sample would promote more reliable and specific PCR-based detection.

In addition to the secondary counter-rotating flow within the cross section of the main channel around the contraction–expansion region, a horizontal micro-vortex within the contraction–expansion chamber can also be generated due to the detachment of the boundary layer under a high flow speed. Shelby *et al.*<sup>87</sup> were among the first to demonstrate a horizontal microvortex in a diamond-shaped cavity under high flow speed in microfluidics. This microvortex can generate a rotational velocity as high as 12  $\text{m s}^{-1}$  and a corresponding radial acceleration in the order of  $10^6 \text{g}$ . Such a microvortex without any moving components is useful for the investigation of the effects of high radial acceleration on biological and chemical processes as well as offering precise control and rotation of a single cell<sup>88</sup> (Fig. 9(a)). In their work, the single cell was actively trapped and positioned at the centre of the microvortex by an optical tweezer.

Later, Di Carlo's group<sup>89,90</sup> introduced the concept of “centrifuge-on-a-chip” to selectively isolate target particles/cells from a heterogeneous background by the effects of inertial migration and vortex trapping. The centrifuge chip consisted of a straight channel section and symmetric expansion–contraction arrays (Fig. 9(b)). Rather than the optical tweezer, the selective trapping and positioning of micro-particles are based on purely hydrodynamic phenomenon: the cross-stream inertial migration of micro-particles in the cavity expanding area. The mechanism of trapping has been qualitatively explained by Mach *et al.*<sup>90</sup> Briefly, the selective trapping process of particles is divided into three steps: (i) inertial focusing in a straight channel, (ii) lateral migration around the expanding area, and (iii) circulation within microvortices (Fig. 9(b)).

The functions of trapping, enrichment, labelling and solution exchange were demonstrated in the centrifuge chip.<sup>90–94</sup> The most significant advantage of “centrifuge-on-a-chip” is its ability to selectively trap particles from the mainstream by size, which is believed to be one of the most size-sensitive separation methods.<sup>59</sup> Di Carlo's group has conducted a series of investigations on its trapping sensitivity and efficiency through a variety of bio-samples, including cancer cells spiked in blood,<sup>90</sup> pleural fluids<sup>92</sup> and blood sample<sup>93</sup> from cancer patients. One possible drawback of this device is that it basically works in a batch procedure, and specifically effective in trapping of rare cells (*e.g.* CTCs), due to the limited capacity in expansion–contraction chambers. Wang *et al.*<sup>91</sup> proposed a modified microvortex-aided device by adding side outlets in each chamber to continuously siphon larger particles from chambers (Fig. 9(c)). However, the device is still limited by the capability for bimodal separation

with a single size cut-off and well-defined size difference. It will become challenging when treating real-world samples that often include heterogeneous mixtures of multiple particle components. Wang and Papautsky<sup>95</sup> developed a multi-modal inertial sorter that consisted of a long straight section with series-connected separation units. The authors successfully demonstrated triple-sized particle separation with high resolution by sequencing two separation units and adjusting the proper system parameters.

Besides the expansion–contraction chamber, a micro-pillar within a micro-channel will also induce irreversible twisted flows at a finite inertial flow. Furthermore, the lateral position of the pillar can be used to tune the position and shape of the net recirculating flows across the channel. It could enable precise control of fluid transformation by programming the positions of sequenced cylindrical pillars (Fig. 9(d)). To explore the capabilities of this sequenced pillar microchannel, Amini *et al.*<sup>26</sup> have successfully demonstrated the sculpture of the cross-sectional shape of a laminated stream into complex geometries, moving and splitting a fluid stream, solution exchange and particle separation. Nunes *et al.*<sup>96</sup> utilized this microfluidic technique to fabricate polymeric microfibers with noncircular cross-sectional shapes (Fig. 9(d)). The computer-aided design (CAD) tool uFlow has a stored library of pre-computed fluid deformations that are produced by individual pillars in the flow channel. It is a useful tool to design pillar sequences and to predict the shape of net flow deformation. The cross-sectional shapes of various fabricated microfibers agreed reasonably well with that of predicted using the uFlow code.

Similar to the secondary flow induced by the contraction–expansion chamber or channel curvature, the locally induced secondary flows by sequenced pillars could also be used to modify the inertial migration progress. Chung *et al.*<sup>97</sup> demonstrated single-stream focusing of microparticles through controllable cross-stream migration, which was aided by the locally tuned secondary flows from the sequential micropillars. Besides, programmable flow deformation in sequential micropillars was used to conduct solution transfer around particles or cells. The microfluidic device was applied for a functionalized bead bioassay, achieving high yield and continuous separation of biotin-coated beads from extra FITC-biotin, as well as extraction of leukocytes from lysed blood.<sup>98</sup>

### 3.4 Serpentine channel

It is known that in spiral channels, the curvature is along a single direction; therefore secondary flow can reach steady state after a given channel length and is almost consistent within different cross sections. Analysis of particle behaviour can be approximated by the static superposition of an inertial lift force field with a secondary flow field. However, in a serpentine channel with alternating curvatures, the situation becomes more sophisticated. For example, with alternating curvatures, secondary flow may not approach steady state

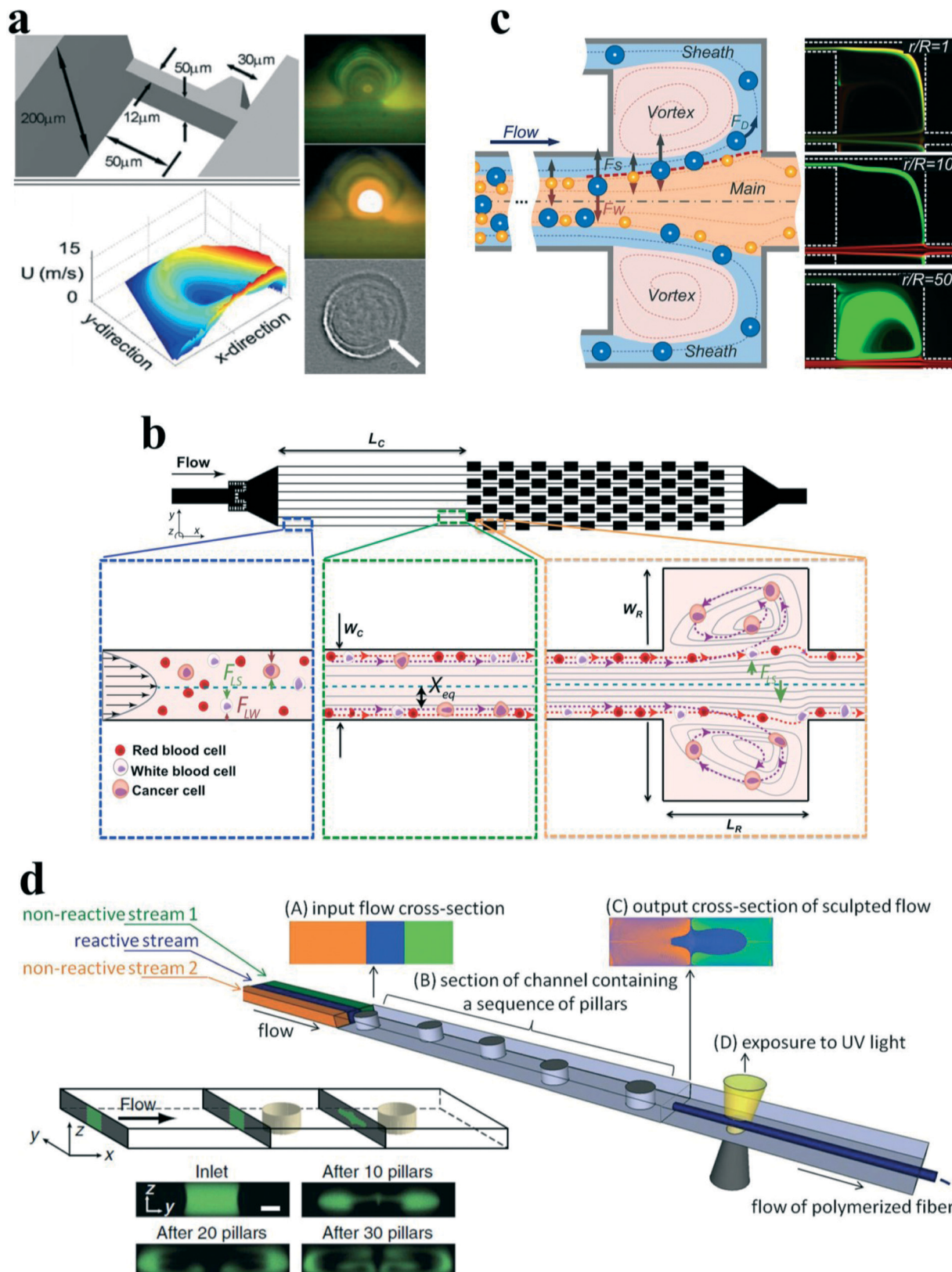


**Fig. 9** (a) Rotational control of single cells by microvortices in a diamond-shaped chamber. Reproduced from ref. 88 with kind permission from Springer Science & Business Media. (b) Size-selective trapping of circulating tumor cells using “centrifuge-on-a-chip”. Reproduced from ref. 93 with permission from the Royal Society of Chemistry. (c) Vortex-aided inertial microfluidic device for continuous sorting of particles by size. A modified side outlet in each chamber siphons the trapped large particles out continuously, meanwhile smaller particles exit from the main channel. Reproduced from ref. 91 with permission from AIP Publishing LLC. (d) Engineering flow deformation by programming a sequence of cylindrical pillars within a straight microchannel in inertial microfluidics and its application on synthesis of shaped polymeric microfibers. Reproduced from ref. 26 and 96 with permission from Nature Publishing Group and John Wiley and Sons, respectively.

after each turn, the same with the movement of particles, and accumulation of this unsteady state may cause unpredictable and non-intuitive behaviour of particles. Therefore, analysis of particle behaviour by the superposition method may not give a convincing explanation.

Di Carlo *et al.*<sup>43</sup> investigated the effects of alternating curvatures on the particle inertial migration. In their study, the original four equilibrium positions in a straight channel with

square cross section were reduced to two in a symmetric serpentine channel due to the symmetry of the system. Above a critical Dean number, focusing was perturbed. Furthermore, in an asymmetric serpentine channel, the number of equilibrium positions could be further reduced to one, and focusing again became more complex as Dean number increased (Fig. 10(a)). From their understanding, the balance between inertial lift forces ( $F_L$ ) and Dean drag force ( $F_D$ ) determines

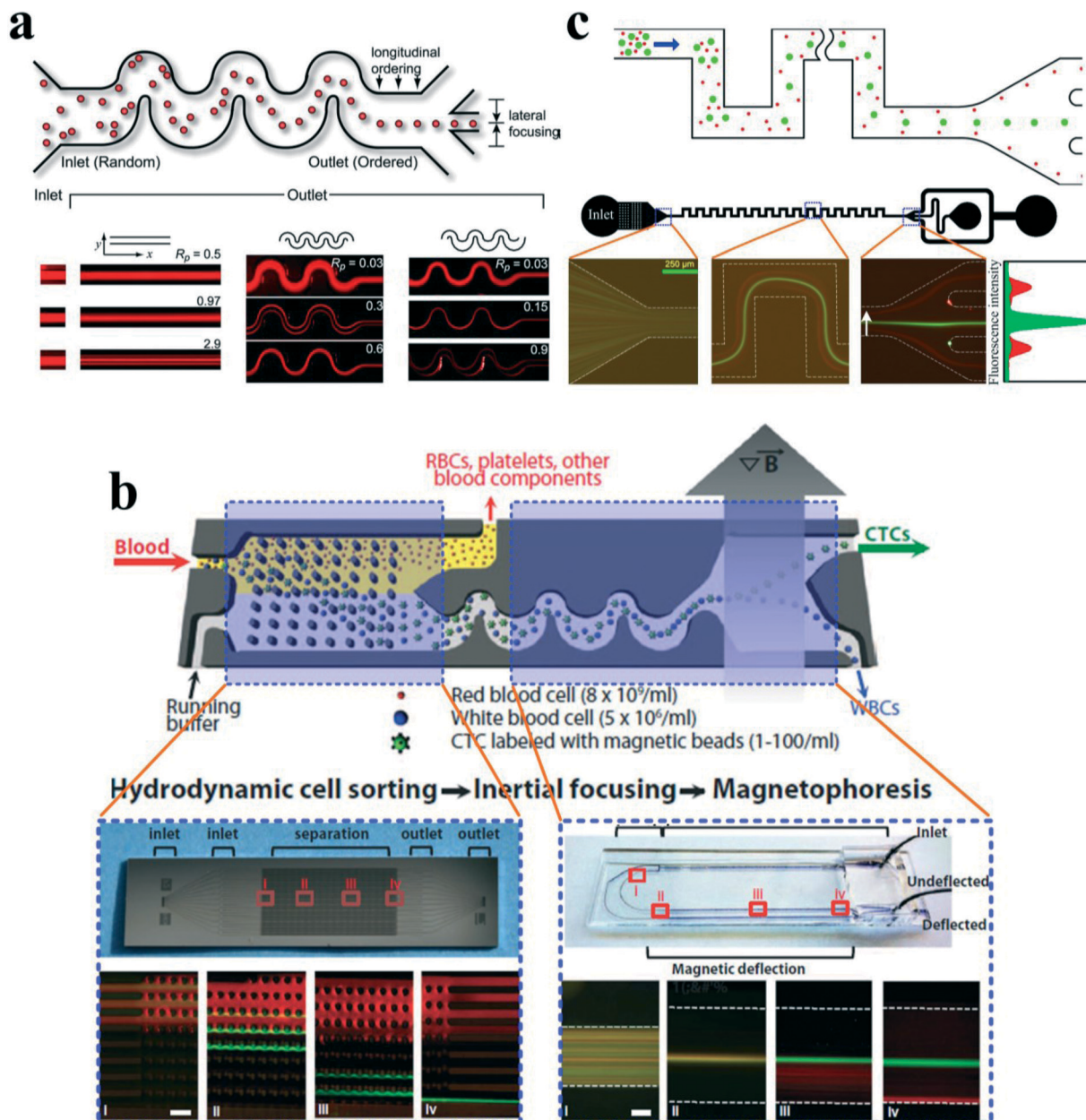


**Fig. 10** (a) Inertial focusing of particles in serpentine microchannels. In a straight channel with a square cross section, focusing of particles into four single streamlines is observed, with each of them facing the centre of each wall. For a symmetric serpentine channel, the symmetry of the system reduces focusing to two streams. In an asymmetric serpentine channel, focusing down to a single stream is observed. Reproduced from ref. 43. Copyright 2007, National Academy of Sciences, USA. (b) A hybrid microfluidic device which integrates deterministic lateral displacement (DLD), inertial focusing in asymmetrical serpentine channel and magnetophoresis (MP) to isolate rare CTCs in an antigen-dependent and -independent way. Reproduced from ref. 101 with permission from the American Association for the Advancement of Science. (c) Size-based separation of binary particles by their differential equilibrium positions in a symmetric serpentine microchannel. Reproduced from ref. 108 with permission from Nature Publishing Group.

the preferred location of focusing positions. Dean flow does not create particle focusing, but it acts in superposition with inertial lift forces to reduce the number of equilibrium positions created by the inertial lift forces. If  $F_D \ll F_L$ , then no focusing will be observed, and if  $F_D \gg F_L$ , then focusing due to inertial lift forces alone will be observed. The ratio of inertial lift force to Dean drag was scaled as

$$F_L/F_D \sim \frac{2R}{H} (a/H)^3 R_e^n, (n < 0).$$

This relation suggests a strong third-power dependence on the ratio of particle to channel dimensions. Even at the same Reynolds number, small particles may be still unfocused independent of channel length because of dominant  $F_D$ , while larger particles quickly become focused. Employing this mechanism, an inertial filtration device using an asymmetrical serpentine channel was developed and tested.<sup>99</sup> Within the expectation, large particles were well focused and small particles below a threshold remained unfocused and randomly distributed. Therefore, large particles were completely removed from the mixture, leaving behind small particles with a high purity (90–100%). However, because small particles are still unfocused, a large number will enter the reservoirs meant for large particles, leading to unsatisfactory purity of the large particle collection.

Inertial focusing in an asymmetric serpentine channel can produce well-defined particle focusing as well as highly regulated inter-particle spacing, which is very promising in a range of applications, *e.g.*, the flow cytometry system,<sup>100</sup> particle active sorting,<sup>101</sup> hydrodynamic stretching of single-cells<sup>102</sup> and bioparticle concentration.<sup>103</sup> Particle inertial focusing may replace the hydrodynamic focusing unit in the standard commercial flow cytometry, composing a compact microfluidic flow cytometry system.<sup>100</sup> Besides, it could also be integrated with an ultrafast optical capturing system for automated flow-through single-cell image analysis.<sup>104</sup> For particle sorting, Toner's group<sup>101,105</sup> developed a hybrid microfluidic device which combined deterministic lateral displacement (DLD), inertial focusing and magnetophoresis (MP) to isolate rare CTCs in an antigen-dependent and -independent way (Fig. 10(b)). In this device, after the sample of raw blood is introduced into the chip, the blood cells first encounter an array of circular pillars with a specific gap, where DLD size-based hydrodynamic force filters smaller red blood cells (RBCs) from white blood cells (WBCs) and CTCs with much larger size. Subsequently, the mixture of WBCs and CTCs flows into an asymmetric serpentine microchannel where it is rapidly aligned along a single path by the inertial effects. At the end of the serpentine channel, a strong magnetic field is applied to deflect those cells that are magnetically labelled. The CTCs can then be collected separately.

Besides the asymmetric serpentine channel, our group has investigated the focusing patterns and corresponding mechanisms in symmetric serpentine channels.<sup>106–108</sup> Three focusing patterns were observed by increasing the flow rate: (i) two-sided focusing, (ii) transitional focusing, and (iii) single central focusing. From our understanding, the secondary

flow due to the channel curvature not only has mixing effects but also can focus particles at the channel centre if the vertical component of secondary flow which is responsible for the mixing effects is suppressed by reducing the aspect ratio of the channel.<sup>106</sup> After that, particles will be focused at the channel lateral centre if the secondary flow is greater than the inertial lift force. In contrast, if the inertial lift force is stronger than the secondary flow, particles will be focused near two sidewalls. If they are in a similar order, particles will be within a transitional focusing pattern, where particles are focused as a wide streak. Employing the overlap of two-sided focusing pattern for small particles and single central focusing pattern for large particles would enable a complete separation by differential lateral equilibrium positions for binary particles<sup>108</sup> (Fig. 10(c)).

A DEP-inertial coupled microfluidic device was proposed through the combination of inertial lift force and DEP force.<sup>109</sup> This combination can modify the inertial focusing patterns in a serpentine channel with a vertical DEP force, which was implemented by interdigitated electrodes patterned on the bottom of the microchannel. By levitating particles towards the vertical centre of the channel by DEP force, the original two-sided focused particles will migrate towards the lateral centre, which indicates that increasing the lateral component of secondary flow drag as well as reducing its vertical component will promote a single central focusing of the particles. This phenomenon further proves that our explanation about inertial focusing in serpentine channels is reasonable. Moreover, this device demonstrated the possibility of combining passive inertial focusing with active DEP to enable more controllability as well as maintaining the advantages of high-throughput.

## 4 Conclusions and outlook

In this review, we first discussed the fundamental dynamics of particle movement. Several lateral forces might act on particles in an inertial microfluidic device. Viscous drag force, arising from the velocity difference between fluid element and particles, basically retains the particles within fluid streamlines. Lateral forces, such as Magnus force, Saffman force, shear gradient lift force and wall lift force, are perpendicular to the main streamlines and account for the intriguing phenomenon of particle inertial migration. In a wall-bounded Poiseuille flow, Magnus and Saffman forces are normally neglected, and the balance of centre-directed wall lift force and wall-directed shear gradient lift force can well explain the experimental observation by Segre and Silberberg.<sup>12,13,17</sup> Besides, the properties of particles (*e.g.* deformability, shape, size) and the fluid property (*e.g.* viscoelasticity) may also influence the lateral migration of particles.<sup>45,49,110</sup>

Subsequently, a comprehensive review of the recent progress of the inertial microfluidic technology was presented according to the structure of functional microchannels, *i.e.* straight,<sup>42,44,49,54</sup> straight channel with pillar arrays<sup>26,97,111</sup> or

expansion–contraction arrays,<sup>25,79,82</sup> spiral,<sup>77,112,113</sup> and serpentine.<sup>43,106,114</sup> These inertial microfluidic devices have been widely explored for their applications in biomedicine and industry, such as extraction of blood plasma,<sup>80,107</sup> separation of particles and cells,<sup>53,68,72,108,115</sup> solution exchange,<sup>98,116,117</sup> cell enrichment,<sup>118</sup> isolation of CTCs,<sup>69,71,75,81,90,92,93,101</sup> detection of malaria pathogen,<sup>86,119</sup> microfiber fabrication,<sup>96</sup> cell cycle synchronization,<sup>73</sup> cell encapsulation,<sup>65</sup> hydrodynamic stretching of single cell,<sup>102,120</sup> etc. There are also several commercial/quasi-commercial prototypes reported based on inertial microfluidic techniques,<sup>35</sup> e.g. CTC-iChip by Johnson & Johnson,<sup>101</sup> ClearCell FX system by Clearbridge BioMedics,<sup>75,121</sup> mechanophenotyping platform by CytoVale,<sup>122</sup> as well as microfluidic “centrifuge-on-a-chip” by Vortex Biosciences.<sup>90,123</sup>

Although there have been extensive investigations on the mechanism of particle inertial focusing, and a variety of applications on particle/cell separation have been demonstrated, quantitative design rules are still lacking for particle inertial manipulation in different shaped channels. Therefore, more dedicated work is needed to uncover the detailed underlying mechanism and provide explicit rules to the end users even without specialized knowledge and experience about inertial microfluidics. In addition, more efforts are needed to improve the separation resolution and processing speed through optimization of channel structure and scale up scheme. Although some parallelization designs can provide good examples<sup>58,76,115,124</sup> a general design guideline and optimization scheme based on different channel structures would be more helpful.

The combination of passive inertial microfluidics with active manipulation techniques will enable a more versatile and powerful functionality. Several manipulation techniques may be connected in series with independent physics, or in parallel with coupled physics. Ozkumur *et al.*<sup>101,105</sup> reported an integrated microfluidic device which combined deterministic lateral displacement (DLD), inertial focusing and magnetophoresis (MP) to isolate rare CTCs in an antigen-dependent and -independent way. Meanwhile, Moon *et al.*<sup>85</sup> successfully separated human breast cancer cells (MCF-7) from spiked blood sample by a combination of multi-orifice flow fractionation (MOFF) and dielectrophoresis (DEP) techniques. In both works, although the physics in each section is common and independent, actually they are weakly linked, because the interface between each section, such as flow rate or pressure, needs to be balanced carefully so that each section can work normally.

We proposed a DEP-inertial microfluidic device, where negative DEP force and inertial lift force are coupled along the vertical direction to adjust the focusing positions of the particles in three dimensions.<sup>109</sup> Based on this platform, the DEP force could be used as a force probe to measure the magnitude of inertial lift force. Besides the DEP force, magnetic, acoustic or other active forces may also be combined with inertial lift force in inertial microfluidics to achieve more versatility and flexibility for microfluidic systems.

Current study on particle manipulation by inertial microfluidics is often limited for particles within the micro-scale region. The territory of nano-scale particles (DNA, protein, virus *etc.*) has not been explored yet in inertial microfluidics. For nano-scale particles, the Brownian motion becomes more obvious and maybe even overcomes its inertial effects. Therefore, a reduced channel size (sub-micron to nano-scale) may not be a necessary consequence, and introduction of additional viscoelastic effects could be a possible alternative.<sup>125</sup>

To date, inertial focusing has been conducted where particles are suspended within the liquid phase. There is no reported work for a particle-air system, *i.e.* aerosol. Whether from the aspects of fundamental exploration on particle movement within micro-airways or from the aspects of its potential application in biomedicine and industry, *e.g.* understanding the functionality of the respiratory system, inhalation drug delivery, air pollution purification, *etc.*, this kind of research is still very meaningful.

In conclusion, although significant progress has been achieved for inertial microfluidics over the last decades, even with a few commercial prototypes developed, inertial microfluidics itself is still in its early development stage. A wide region of its raw territory has been waiting for exploration and exploitation. We believe that in the near future inertial microfluidics will remain a hot research topic with expanding applications because of the superior advantages of the technology, such as high throughput, simple structure and low cost.

## Acknowledgements

This work was partially supported by the University of Wollongong through a UIC grant and China Scholarship Council.

## References

- 1 G. M. Whitesides, *Nature*, 2006, **442**, 368–373.
- 2 E. K. Sackmann, A. L. Fulton and D. J. Beebe, *Nature*, 2014, **507**, 181–189.
- 3 A. A. S. Bhagat, H. Bow, H. W. Hou, S. J. Tan, J. Han and C. T. Lim, *Med. Biol. Eng. Comput.*, 2010, **48**, 999–1014.
- 4 D. Di Carlo, *Lab Chip*, 2009, **9**, 3038–3046.
- 5 A. J. Mach, O. B. Adeyiga and D. Di Carlo, *Lab Chip*, 2013, **13**, 1011–1026.
- 6 B. Çetin and D. Li, *Electrophoresis*, 2011, **32**, 2410–2427.
- 7 T. P. Forbes and S. P. Forry, *Lab Chip*, 2012, **12**, 1471–1479.
- 8 Z. Wang and J. Zhe, *Lab Chip*, 2011, **11**, 1280–1285.
- 9 D. G. Grier, *Nature*, 2003, **424**, 810–816.
- 10 M. Yamada, M. Nakashima and M. Seki, *Anal. Chem.*, 2004, **76**, 5465–5471.
- 11 L. R. Huang, E. C. Cox, R. H. Austin and J. C. Sturm, *Science*, 2004, **304**, 987–990.
- 12 G. Segre, *Nature*, 1961, **189**, 209–210.
- 13 G. Segre and A. Silberberg, *J. Fluid Mech.*, 1962, **14**, 136–157.
- 14 J. B. McLaughlin, *J. Fluid Mech.*, 1993, **246**, 249–265.

- 15 D. D. Joseph and D. Ocando, *J. Fluid Mech.*, 2002, **454**, 263–286.
- 16 P. Cherukat and J. B. McLaughlin, *J. Fluid Mech.*, 1994, **263**, 1–18.
- 17 E. S. Asmolov, *J. Fluid Mech.*, 1999, **381**, 63–87.
- 18 B. Chun and A. Ladd, *Phys. Fluids*, 2006, **18**, 031704.
- 19 T. Tanaka, T. Ishikawa, K. Numayama-Tsuruta, Y. Imai, H. Ueno, T. Yoshimoto, N. Matsuki and T. Yamaguchi, *Biomed. Microdevices*, 2012, **14**, 25–33.
- 20 B. H. Yang, J. Wang, D. D. Joseph, H. H. Hu, T.-W. Pan and R. Glowinski, *J. Fluid Mech.*, 2005, **540**, 109–131.
- 21 K. Hood, S. Lee and M. Roper, *J. Fluid Mech.*, 2015, **765**, 452–479.
- 22 J.-P. Matas, J. F. Morris and É. Guazzelli, *J. Fluid Mech.*, 2004, **515**, 171–195.
- 23 S. Berger, L. Talbot and L. Yao, *Annu. Rev. Fluid Mech.*, 1983, **15**, 461–512.
- 24 M. G. Lee, S. Choi and J. K. Park, *Appl. Phys. Lett.*, 2009, **95**, 051902.
- 25 J. Zhang, M. Li, W. Li and G. Alici, *J. Micromech. Microeng.*, 2013, **23**, 085023.
- 26 H. Amini, E. Sollier, M. Masaeli, Y. Xie, B. Ganapathysubramanian, H. A. Stone and D. Di Carlo, *Nat. Commun.*, 2013, **4**, 1826.
- 27 J. F. Richardson, J. M. Coulson, J. Harker and J. Backhurst, *Chemical Engineering: Particle technology and separation processes*, Butterworth-Heinemann, 2002.
- 28 R. M. Mazo, *Brownian motion: fluctuations, dynamics, and applications*, Clarendon press Oxford, 2002.
- 29 R. Clift, J. R. Grace and M. E. Weber, *Bubbles, drops, and particles*, Courier Corporation, 2005.
- 30 E. Michaelides, *Particles, bubbles & drops: their motion, heat and mass transfer*, World Scientific, Singapore, 2006.
- 31 S. Rubinow and J. B. Keller, *J. Fluid Mech.*, 1961, **11**, 447–459.
- 32 J. Matas, J. Morris and E. Guazzelli, *Oil Gas Sci. Technol.*, 2004, **59**, 59–70.
- 33 J. Feng, H. H. Hu and D. D. Joseph, *J. Fluid Mech.*, 1994, **277**, 271–301.
- 34 P. G. Saffman, *J. Fluid Mech.*, 1965, **22**, 385–400.
- 35 H. Amini, W. Lee and D. Di Carlo, *Lab Chip*, 2014, **14**, 2739–2761.
- 36 Y. W. Kim and J. Y. Yoo, *Lab Chip*, 2009, **9**, 1043–1045.
- 37 H. Brenner, *Chem. Eng. Sci.*, 1961, **16**, 242–251.
- 38 R. Cox and S. Hsu, *Int. J. Multiphase Flow*, 1977, **3**, 201–222.
- 39 P. Vasseur and R. G. Cox, *J. Fluid Mech.*, 1977, **80**, 561–591.
- 40 P. Cherukat and J. McLaughlin, *Int. J. Multiphase Flow*, 1990, **16**, 899–907.
- 41 A. A. S. Bhagat, S. S. Kuntaegowdanahalli and I. Papautsky, *Microfluid. Nanofluid.*, 2009, **7**, 217–226.
- 42 J. Zhou and I. Papautsky, *Lab Chip*, 2013, **13**, 1121–1132.
- 43 D. Di Carlo, D. Irimia, R. G. Tompkins and M. Toner, *Proc. Natl. Acad. Sci. U. S. A.*, 2007, **104**, 18892–18897.
- 44 D. Di Carlo, J. F. Edd, K. J. Humphry, H. A. Stone and M. Toner, *Phys. Rev. Lett.*, 2009, **102**, 94503.
- 45 S. C. Hur, N. K. Henderson-MacLennan, E. R. McCabe and D. Di Carlo, *Lab Chip*, 2011, **11**, 912–920.
- 46 C. A. Stan, A. K. Ellerbee, L. Guglielmini, H. A. Stone and G. M. Whitesides, *Lab Chip*, 2013, **13**, 365–376.
- 47 P.-H. Chan and L. Leal, *J. Fluid Mech.*, 1979, **92**, 131–170.
- 48 H. W. Hou, A. A. S. Bhagat, A. G. L. Chong, P. Mao, K. S. W. Tan, J. Han and C. T. Lim, *Lab Chip*, 2010, **10**, 2605–2613.
- 49 S. C. Hur, S.-E. Choi, S. Kwon and D. Di Carlo, *Appl. Phys. Lett.*, 2011, **99**, 044101.
- 50 E. J. Lim, T. J. Ober, J. F. Edd, S. P. Desai, D. Neal, K. W. Bong, P. S. Doyle, G. H. McKinley and M. Toner, *Nat. Commun.*, 2014, **5**, 4120.
- 51 Y.-S. Choi, K.-W. Seo and S.-J. Lee, *Lab Chip*, 2011, **11**, 460–465.
- 52 A. J. Chung, D. R. Gossett and D. Di Carlo, *Small*, 2013, **9**, 685–690.
- 53 M. G. Lee, S. Choi and J. K. Park, *J. Chromatogr. A*, 2011, **1218**, 4138–4143.
- 54 H. Amini, E. Sollier, W. M. Weaver and D. Di Carlo, *Proc. Natl. Acad. Sci. U. S. A.*, 2012, **109**, 11593–11598.
- 55 W. Lee, H. Amini, H. A. Stone and D. Di Carlo, *Proc. Natl. Acad. Sci. U. S. A.*, 2010, **107**, 22413–22418.
- 56 C. Liu, G. Hu, X. Jiang and J. Sun, *Lab Chip*, 2015, **15**, 1168–1177.
- 57 S. C. Hur, T. Z. Brinckerhoff, C. M. Walthers, J. C. Dunn and D. Di Carlo, *PLoS One*, 2012, **7**, e46550.
- 58 A. J. Mach and D. Di Carlo, *Biotechnol. Bioeng.*, 2010, **107**, 302–311.
- 59 J. Zhou, P. V. Giridhar, S. Kasper and I. Papautsky, *Lab Chip*, 2013, **13**, 1919–1929.
- 60 J. S. Dudani, D. E. Go, D. R. Gossett, A. P. Tan and D. Di Carlo, *Anal. Chem.*, 2014, **86**, 1502–1510.
- 61 A. P. Tan, J. S. Dudani, A. Arshi, R. J. Lee, T. Henry, D. R. Gossett and D. Di Carlo, *Lab Chip*, 2014, **14**, 522–531.
- 62 S. C. Hur, H. T. K. Tse and D. Di Carlo, *Lab Chip*, 2010, **10**, 274–280.
- 63 T. M. Squires and S. R. Quake, *Rev. Mod. Phys.*, 2005, **77**, 977.
- 64 A. A. S. Bhagat, S. S. Kuntaegowdanahalli, N. Kaval, C. J. Seliskar and I. Papautsky, *Biomed. Microdevices*, 2010, **12**, 187–195.
- 65 E. W. Kemna, R. M. Schoeman, F. Wolbers, I. Vermes, D. A. Weitz and A. van den Berg, *Lab Chip*, 2012, **12**, 2881–2887.
- 66 D. H. Yoon, J. B. Ha, Y. K. Bahk, T. Arakawa, S. Shoji and J. S. Go, *Lab Chip*, 2008, **9**, 87–90.
- 67 A. A. S. Bhagat, S. S. Kuntaegowdanahalli and I. Papautsky, *Lab Chip*, 2008, **8**, 1906–1914.
- 68 S. S. Kuntaegowdanahalli, A. A. S. Bhagat, G. Kumar and I. Papautsky, *Lab Chip*, 2009, **9**, 2973–2980.
- 69 J. Sun, M. Li, C. Liu, Y. Zhang, D. Liu, W. Liu, G. Hu and X. Jiang, *Lab Chip*, 2012, **12**, 3952–3960.
- 70 J. Sun, C. Liu, M. Li, J. Wang, Y. Xianyu, G. Hu and X. Jiang, *Biomicrofluidics*, 2013, **7**, 011802.
- 71 M. E. Warkiani, G. Guan, K. B. Luan, W. C. Lee, A. A. S. Bhagat, P. K. Chaudhuri, D. S.-W. Tan, W. T. Lim, S. C. Lee and P. C. Chen, *Lab Chip*, 2014, **14**, 128–137.

- 72 L. Wu, G. Guan, H. W. Hou, A. A. S. Bhagat and J. Han, *Anal. Chem.*, 2012, **84**, 9324–9331.
- 73 W. C. Lee, A. A. S. Bhagat, S. Huang, K. J. Van Vliet, J. Han and C. T. Lim, *Lab Chip*, 2011, **11**, 1359–1367.
- 74 W. Sheng, T. Chen, R. Kamath, X. Xiong, W. Tan and Z. H. Fan, *Anal. Chem.*, 2012, **84**, 4199–4206.
- 75 H. W. Hou, M. E. Warkiani, B. L. Khoo, Z. R. Li, R. A. Soo, D. S.-W. Tan, W.-T. Lim, J. Han, A. A. S. Bhagat and C. T. Lim, *Sci. Rep.*, 2013, **3**, 1259.
- 76 M. E. Warkiani, B. L. Khoo, D. S.-W. Tan, A. A. S. Bhagat, W.-T. Lim, Y. S. Yap, S. C. Lee, R. A. Soo, J. Han and C. T. Lim, *Analyst (Cambridge, U.K.)*, 2014, **139**, 3245–3255.
- 77 G. Guan, L. Wu, A. A. Bhagat, Z. Li, P. C. Chen, S. Chao, C. J. Ong and J. Han, *Sci. Rep.*, 2013, **3**, 1475.
- 78 B. L. Khoo, M. E. Warkiani, D. S.-W. Tan, A. A. S. Bhagat, D. Irwin, D. P. Lau, A. S. Lim, K. H. Lim, S. S. Krisna and W.-T. Lim, *PLoS One*, 2014, **9**, e99409.
- 79 M. G. Lee, S. Choi and J. K. Park, *Lab Chip*, 2009, **9**, 3155–3160.
- 80 M. G. Lee, S. Choi, H. J. Kim, H. K. Lim, J. H. Kim, N. Huh and J. K. Park, *Appl. Phys. Lett.*, 2011, **98**, 253702.
- 81 M. G. Lee, J. H. Shin, C. Y. Bae, S. Choi and J.-K. Park, *Anal. Chem.*, 2013, **85**, 6213–6218.
- 82 J. S. Park, S. H. Song and H. I. Jung, *Lab Chip*, 2009, **9**, 939–948.
- 83 J.-S. Park and H.-I. Jung, *Anal. Chem.*, 2009, **81**, 8280–8288.
- 84 T. S. Sim, K. Kwon, J. C. Park, J.-G. Lee and H.-I. Jung, *Lab Chip*, 2011, **11**, 93–99.
- 85 H. S. Moon, K. Kwon, S. I. Kim, H. Han, J. Sohn, S. Lee and H. I. Jung, *Lab Chip*, 2011, **11**, 1118–1125.
- 86 M. E. Warkiani, A. K. P. Tay, B. L. Khoo, X. Xiaofeng, J. Han and C. T. Lim, *Lab Chip*, 2015, **15**, 1101–1109.
- 87 J. P. Shelby, D. S. Lim, J. S. Kuo and D. T. Chiu, *Nature*, 2003, **425**, 38–38.
- 88 D. T. Chiu, *Anal. Bioanal. Chem.*, 2007, **387**, 17–20.
- 89 S. C. Hur, A. J. Mach and D. Di Carlo, *Biomicrofluidics*, 2011, **5**, 022206.
- 90 A. J. Mach, J. H. Kim, A. Arshi, S. C. Hur and D. Di Carlo, *Lab Chip*, 2011, **11**, 2827–2834.
- 91 X. Wang, J. Zhou and I. Papautsky, *Biomicrofluidics*, 2013, **7**, 044119.
- 92 J. Che, A. J. Mach, D. E. Go, I. Talati, Y. Ying, J. Rao, R. P. Kulkarni and D. Di Carlo, *PLoS One*, 2013, **8**, e78194.
- 93 E. Sollier, D. E. Go, J. Che, D. R. Gossett, S. O'Byrne, W. M. Weaver, N. Kummer, M. Rettig, J. Goldman and N. Nickols, *Lab Chip*, 2014, **14**, 63–77.
- 94 J. Zhou, S. Kasper and I. Papautsky, *Microfluid. Nanofluid.*, 2013, **15**, 611–623.
- 95 X. Wang and I. Papautsky, *Lab Chip*, 2015, **15**, 1350–1359.
- 96 J. K. Nunes, C. Y. Wu, H. Amini, K. Owsley, D. Di Carlo and H. A. Stone, *Adv. Mater.*, 2014, **26**, 3712–3717.
- 97 A. J. Chung, D. Pulido, J. C. Oka, H. Amini, M. Masaeli and D. Di Carlo, *Lab Chip*, 2013, **13**, 2942–2949.
- 98 E. Sollier, H. Amini, D. Go, P. Sandoz, K. Owsley and D. Di Carlo, *Microfluid. Nanofluid.*, 2015, **19**, 53–65.
- 99 D. Di Carlo, F. Jon, D. Irimia, R. G. Tompkins and M. Toner, *Anal. Chem.*, 2008, **80**, 2204–2211.
- 100 J. Oakey, R. W. ApplegateJr, E. Arellano, D. D. Carlo, S. W. Graves and M. Toner, *Anal. Chem.*, 2010, **82**, 3862–3867.
- 101 E. Ozkumur, A. M. Shah, J. C. Ciciliano, B. L. Emmink, D. T. Miyamoto, E. Brachtel, M. Yu, P.-I. Chen, B. Morgan and J. Trautwein, *Sci. Transl. Med.*, 2013, **5**, 179ra147.
- 102 D. R. Gossett, T. Henry, S. A. Lee, Y. Ying, A. G. Lindgren, O. O. Yang, J. Rao, A. T. Clark and D. Di Carlo, *Proc. Natl. Acad. Sci. U. S. A.*, 2012, **109**, 7630–7635.
- 103 J. M. Martel, K. C. Smith, M. Dlamini, K. Pletcher, J. Yang, M. Karabacak, D. A. Haber, R. Kapur and M. Toner, *Sci. Rep.*, 2015, **5**, 11300.
- 104 K. Goda, A. Ayazi, D. R. Gossett, J. Sadashivam, C. K. Lonappan, E. Sollier, A. M. Fard, S. C. Hur, J. Adam and C. Murray, *Proc. Natl. Acad. Sci. U. S. A.*, 2012, **109**, 11630–11635.
- 105 N. M. Karabacak, P. S. Spuhler, F. Fachin, E. J. Lim, V. Pai, E. Ozkumur, J. M. Martel, N. Kojic, K. Smith and P.-I. Chen, *Nat. Protoc.*, 2014, **9**, 694–710.
- 106 J. Zhang, W. Li, M. Li, G. Alici and N.-T. Nguyen, *Microfluid. Nanofluid.*, 2013, **17**, 305–316.
- 107 J. Zhang, S. Yan, W. Li, G. Alici and N.-T. Nguyen, *RSC Adv.*, 2014, **4**, 33149–33159.
- 108 J. Zhang, S. Yan, R. Sluyter, W. Li, G. Alici and N.-T. Nguyen, *Sci. Rep.*, 2014, **4**, 4527.
- 109 J. Zhang, S. Yan, G. Alici, N.-T. Nguyen, D. Di Carlo and W. Li, *RSC Adv.*, 2014, **4**, 62076–62085.
- 110 F. Del Giudice, G. Romeo, G. D'Avino, F. Greco, P. A. Netti and P. L. Maffettone, *Lab Chip*, 2013, **13**, 4263–4271.
- 111 D. Stoecklein, C.-Y. Wu, K. Owsley, Y. Xie, D. Di Carlo and B. GanapathySubramanian, *Lab Chip*, 2014, **14**, 4197–4204.
- 112 N. Xiang, H. Yi, K. Chen, D. Sun, D. Jiang, Q. Dai and Z. Ni, *Biomicrofluidics*, 2013, **7**, 044116.
- 113 J. M. Martel and M. Toner, *Sci. Rep.*, 2013, **3**, 3340.
- 114 D. R. Gossett and D. D. Carlo, *Anal. Chem.*, 2009, **81**, 8459–8465.
- 115 M. E. Warkiani, A. K. P. Tay, G. Guan and J. Han, *Sci. Rep.*, 2015, **5**, 11018.
- 116 J. S. Dudani, D. R. Gossett, T. Henry, R. J. Lamm, R. P. Kulkarni and D. Di Carlo, *Biomicrofluidics*, 2015, **9**, 014112.
- 117 D. R. Gossett, H. T. K. Tse, J. S. Dudani, K. Goda, T. A. Woods, S. W. Graves and D. Di Carlo, *Small*, 2012, **8**, 2757–2764.
- 118 J. M. Martel, K. C. Smith, M. Dlamini, K. Pletcher, J. Yang, M. Karabacak, D. A. Haber, R. Kapur and M. Toner, *Sci. Rep.*, 2015, **5**, 11300.
- 119 C. M. Birch, H. W. Hou, J. Han and J. C. Niles, *Sci. Rep.*, 2015, **5**, 11347.
- 120 J. S. Dudani, D. R. Gossett, T. Henry and D. Di Carlo, *Lab Chip*, 2013, **13**, 3728–3734.
- 121 C. BioMedics, *Clearcell FX System*, <http://www.clearbridgebiomedics.com/>, Accessed 28th Oct, 2015.

- 122 T. Henry, D. R. Gossett, Y. S. Moon, M. Masaeli, M. Sohsman, Y. Ying, K. Mislick, R. P. Adams, J. Rao and D. Di Carlo, *Sci. Transl. Med.*, 2013, 5, 212ra163.
- 123 V. Biosciences, *Vortex technology/microfluidic "centrifuge-on-a-chip"*, <http://www.vortexbiosciences.com/>, Accessed 28th Oct, 2015.
- 124 J. Hansson, J. M. Karlsson, T. Haraldsson, H. Brismar, W. van der Wijngaart and A. Russom, *Lab Chip*, 2012, 12, 4644–4650.
- 125 J. Y. Kim, S. W. Ahn, S. S. Lee and J. M. Kim, *Lab Chip*, 2012, 12, 2807–2814.